UNIVERSIDADE ESTADUAL DE CAMPINAS
FACULDADE DE ENGENHARIA ELÉTRICA E DE COMPUTAÇÃO

Rafael Fernandes Alvarenga

Modal Content Characterization in Few-Mode Fibers Using Spatially and Spectrally Resolved Imaging

Caracterização de Conteúdo Modal em Fibras de Poucos Modos Usando Imageamento Espacial e Espectral

Campinas
2022

Rafael Fernandes Alvarenga

Modal Content Characterization in Few-Mode Fibers Using Spatially and Spectrally Resolved Imaging

Caracterização de Conteúdo Modal em Fibras de Poucos Modos Usando Imageamento Espacial e Espectral

Dissertation presented to the School of Electrical and Computer Engineering of the University of Campinas in partial fulfillment of the requirements for the degree of Master in Electrical Enginnering, in the Area of Telecommunications and Telematics.

Dissertação apresentada à Faculdade de Engenharia Elétrica e de Computação da Universidade Estadual de Campinas como parte dos requisitos exigidos para a obtenção do título de Mestre em Engenharia Elétrica, na Àrea de Telecomunicações e Telemática

Advisor/Orientador: Prof. Dr. Lucas Heitzmann Gabrielli

Este trabalho corresponde à versão final da dissertação defendida pelo aluno Rafael Fernandes Alvarenga, e orientada pelo Prof. Dr. Lucas Heitzmann Gabrielli.

Campinas
2022

Ficha catalográfica
Universidade Estadual de Campinas
Biblioteca da Área de Engenharia e Arquitetura
Elizangela Aparecida dos Santos Souza - CRB 8/8098

Al86m

Alvarenga, Rafael Fernandes, 1994-
Modal content characterization in few-mode fibers using spatially and spectrally resolved imaging / Rafael Fernandes Alvarenga. – Campinas, SP : [s.n.], 2022.

Orientador: Lucas Heitzmann Gabrielli.
Dissertação (mestrado) – Universidade Estadual de Campinas, Faculdade de Engenharia Elétrica e de Computação.

1. Tecnologia de fibra óptica. 2. Espectrometro de imageamento. I. Gabrielli, Lucas Heitzmann, 1982-. II. Universidade Estadual de Campinas. Faculdade de Engenharia Elétrica e de Computação. III. Título.

Informações para Biblioteca Digital

Título em outro idioma: Caracterização de conteúdo modal em fibras de poucos modos usando imageamento espacial e espectral
Palavras-chave em inglês:
Optical fiber technology
Spectral imaging
Área de concentração: Telecomunicações e Telemática
Titulação: Mestre em Engenharia Elétrica
Banca examinadora:
Lucas Heitzmann Gabrielli [Orientador]
Hugo Enrique Hernandez Figueroa
Felippe Alexandre Silva Barbosa
Data de defesa: 02-06-2022
Programa de Pós-Graduação: Engenharia Elétrica

Identificação e informações acadêmicas do(a) aluno(a)
- ORCID do autor: 0000-0001-5214-2594
- Currículo Lattes do autor: http://lattes.cnpq.br/4231440865238518

Comissão Julgadora – Dissertação de Mestrado

Candidato: Rafael Fernandes Alvarenga **RA:** 262735

Data da Defesa: 02 de junho de 2022

Título da Tese: "Modal Content Characterization in Few-Mode Fibers Using Spatially and Spectrally Resolved Imaging (Caracterização de Conteúdo Modal em Fibras de Poucos Modos Usando Imageamento Espacial e Espectral)."

Prof. Dr. Lucas Heitzmann Gabrielli (Presidente, FEEC/UNICAMP)
Prof. Dr. Hugo Enrique Hernandez Figueroa (FEEC/UNICAMP)
Prof. Dr. Felippe Alexandre Silva Barbosa (IFGW/UNICAMP)

A ata de defesa, com as respectivas assinaturas dos membros da Comissão Julgadora, encontra-se no SIGA (Sistema de Fluxo de Dissertação/Tese) e na Secretaria de Pós-Graduação da Faculdade de Engenharia Elétrica e de Computação.

Acknowledgements

First of all, I want to thank God, my Father who always gave me grace in the hard moments. I thank the love of my life, my wife Flavia, who always was by my side of uncountable ways. My parents, Valterlei and Denaide, for supporting me through this years. This achievement belongs to all of you.

I also thank my friend Alexander Isac for motivating me to leave my hometown and join the Master's program in UNICAMP. And Emerson, for its friendship since undergraduate degree at UFT.

I thank my friends, Paulo Jarschel, Erick and Lucas for their experience and knowledge. You were so important for my studies and execution of the experiments. I really thank you so much for companionship.

A special thanks to my advisor, Prof. Lucas Gabrielli. In 2019, I was very well received in his office. We talked about the research project and visited the laboratory. I really felt welcomed. During all the program, his pattient and support were essentials. Thank you for your knowledge and scientific qualities.

I thank Corning Incorporated for providing the fiber used in this work. FAPESP and CAPES have my gratitude for supporting this work by providing equipped laboratories with the best instruments and components. This study was financed in part by the Coordenação de Aperfeiçoamento de Pessoal de Nível Superior - Brasil (CAPES) - Finance Code: 001.

Our greatest weakness lies in giving up.
The most certain way to succeed is always to try just one more time.
Thomas A. Edison

Resumo

O crescente aumento no uso da Internet e outras tecnologias na área da telecomunicação tem elevado significativamente o tráfego de dados em todo o mundo. Além disso, a pandemia COVID19 é um fato recente que maximizou esse cenário devido à transição para atividades remotas. E portanto, os sistemas de comunicações ópticos atuais, sobretudo as redes ópticas baseadas majoritariamente em fibras monomodos (SMFs), que estão no limite teórico de sua capacidade de transmissão, podem não ser capazes de absorver a demanda prevista. Isso impulsiona o desenvolvimento de sistemas baseados em multiplexação por divisão espacial (SDM), nos quais a fibra óptica de poucos modos (FMF) tem uma importante aplicação. Além disso, o desenvolvimento de dispositivos multimodo que podem ser implementados em aplicações de multiplexação por divisão modal (MDM) é de suma importância para a comunidade científica. Visando recuperar informações referentes aos diferentes modos de propagação da luz nesse tipo de dispositivos, o método de Imageamento Espacial e Espectral (S^2) foi aplicado para realizar a caracterização do conteúdo modal da FMF em estudo. Esse método de caracterização baseia-se no princípio de que os modos propagantes viajam com velocidades de grupo diferentes ao longo do comprimento da fibra, logo é possível recuperá-los através do padrão de interferência gerado devido ao atraso de propagação entre os modos. Concluída essa primeira etapa, o método S^2 também foi implementado para caracterizar o conteúdo modal na saída da fibra quando era excitada por um acoplador integrado de três modos com o objetivo de validar a operação do dispositivo. Esse acoplador, desenvolvido pelo Grupo de Eletromagnetismo Aplicado e Computacional (GEMAC), foi construído em uma plataforma de silício encapsulado (SOI). Resultados convincentes foram obtidos em ambas as abordagens experimentais. Na literatura são listados diferentes métodos para análise de conteúdo modal. Neste trabalho, optou-se pelo o método S^2 sobretudo porque ele não impõe um conhecimento prévio do perfil óptico modal da fibra em estudo e não exige técnicas interferométricas na configuração experimental, simplificando a sua implementação.

Abstract

The growing increase of Internet users and others technologies related to the telecommunication field have boosted the data traffic around the world. Moreover, the COVID19 pandemic is a recent fact that has maximized this scenario due to the transition to remote activities. Thus, the current optical communications systems, especially the optical networks based mostly on single-mode fibers (SMFs), which are at its theoretical transmission capacity limit, could not be able to absorb the forecasted demand. This drives the development of systems based on Space-Division Multiplexing (SDM), in which the few-mode fiber (FMF) has an important application. Furthermore, the development of multimode devices for implementation in mode-division multiplexing (MDM) applications plays a key role for scientific community. In order to recover different light propagation modes information in this type of devices, we applied the Spatially and Spectrally Resolved Imaging (S^2) method to execute the modal content characterization of the FMF under test. This characterization method is based on the principle that the propagating modes travel with different group velocities along the fiber length, thus it is possible to recover them from the interference pattern generated due to the differential group delay (DGD) between the modes. After that, S^2 method was also implemented to characterize the modal content at the fiber output when is excited by a tri-modal integrated coupler in order to validate the operation of the device. This coupler, developed by Applied and Computational Electromagnetics Group (GEMAC), was built in a Silicon-On-Insulator (SOI) platform. Robust results were achieved on both experimental approaches by applying the method. In the literature are listed different methods to analyze the modal content. In this work, the S^2 method was chosen because it does not impose a prior knowledge of the optical mode profile of the fiber under test (FUT) and do not need interferometric techniques on the experimental setup, which simplifies its implementation.

List of Figures

List of Tables

Abbreviations

BE	beam expander
C²	Cross-correlated Imaging
CAD	computer aided design
CCD	charge-coupled device
CMOS	complementary metal-oxide semiconductor
DCI	data center interconnect
DGD	differential group delay
DSP	digital signal processing
DWDM	dense wavelength division multiplexing
EDF	erbium-doped fiber
EDFA	erbium-doped fiber amplifier
FEM	Finite Element Method
FMF	few-mode fiber
FUT	fiber under test
GEMAC	Applied and Computational Electromagnetics Group
HC-PCF	hollow-core photonic crystal fiber
HOE	holographic optical element
HOM	higher-order mode
IFT	Inverse Fourier Transform
IoT	Internet of Things
LCO	Optical Communications Laboratory
LEMAC	Laboratory of Applied and Computational Electromagnetics
LMA	large-mode-area
LP	linearly polarized

MCF multi-core fiber

MDL mode-dependent loss

MDM mode-division multiplexing

MIMO multiple-input multiple-output

MMF multimode fiber

MPI Multi-Path Interference

OSA optical spectrum analyzer

OWC optical wireless communication

PC polarization controller

Photonicamp Photonics Research Center

PIC photonic integrated circuit

S^2 Spatially and Spectrally Resolved Imaging

SBS stimulated Brillouin scattering

SDM Space-Division Multiplexing

SiPh Silicon Photonics

SLM spatial light modulator

SMF single-mode fiber

SOI Silicon-On-Insulator

SoP state of polarization

SRS stimulated Raman scattering

TE transverse electric

TLS tunable laser source

WDM wavelength division multiplexing

Summary

Chapter 1

Introduction

1.1 An overview of optical communication systems

The growing demand for data traffic around the world has driven the development of the optical communication systems over the years. In the 1970s, the first optical systems were built using GaAs semiconductor lasers and multimode fibers (MMFs), operating in the spectral region near 0.8 µm [1]. After many efforts, such systems were commercially implemented in 1980 [2]. They achieved a bit rate of 45 Mb/s with 20 dB/km attenuation loss, leading to repeater spacing of up to 10 km, an improvement from the existing coaxial systems that needed spacing ten times larger.

In the early 1980s, InGaAs semiconductor lasers and detectors were developed enabling the operation in the spectral region near 1.3 µm in which the available MMFs exhibited less attenuation losses. So that, the repeater spacing could be increased up to 25 km at a bit rate of 90 Mb/s [2] and up to few hundreds of megabits per second with smaller repeater spacing [3]. However, the attenuation losses and dispersion in MMFs were still the limiting factor.

The continuous improvement of the manufacturing processes allowed to overcome the limitation caused by the dispersion with the application of single-mode fibers (SMFs). This kind of fiber had a smaller core radius than the MMF and supported only one propagating mode at 1.3 µm, what reduced the fiber losses to values below 1 dB/km [4, 5]. As a result, a laboratory experiment in 1981 achieved an optical signal transmission at bit rate of 2 Gb/s over 44 km SMF link [6]. Later, in the late 1980s, when these systems were commercially available, they operated with a repeater spacing of 50 km approximately at bit rates of up to 1.7 Gb/s [1].

Nevertheless, the repeater spacing could not be further enhanced due to the attenuation losses. The solution to that was to migrate to another operation region near 1.55 µm where the SMF attenuation loss is 0.2 dB/km [7]. This change was followed by two innovations: first, the application of the dispersion-shifted fibers in some systems that

were developed to have minimum dispersion near 1.55 µm. Second, the improvement of the lasers that became able to operate by oscillating in a single longitudinal mode while the previous technology operated with simultaneous oscillation of several longitudinal modes resulting in pulse spreading [1]. With both improvements, in 1985, a laboratory experiment demonstrated an optical signal transmission at a bit rate of 4 Gb/s over 103 km SMF link [8]. In 1990, such systems became commercially available operating at 2.5 Gb/s.

Despite these improvements, the necessity of several electronic repeaters in the optical link was still the biggest limiting factor to solve, because they were responsible to increase the transmission costs. One attempt to solve this barrier was to increase the repeater spacing by the improvement of the receiver sensitivity with homodyne and heterodyne detection techniques, the coherent detection for optical systems [9]. Experiments in the 1980s demonstrated the advantages of these techniques [10], but such systems were not commercially implemented at that time, once a revolution in the optical systems communications happened with the advent of the fiber amplifiers and the wavelength division multiplexing (WDM).

In 1989 [11], the erbium-doped fiber amplifier (EDFA) took an important place in optical communications, allowing the transmission of an optical signal for long distances with no need for optoelectronic conversions. At that time, the electronic repeater needed to convert the input optical signal to the electronic domain, amplify it and then to convert the eletronic amplified signal to the optical domain again, getting an amplified output optical signal. With the advent of EDFA, all amplification process could be done in the optical domain by using a loop of few meters erbium-doped fiber (EDF) and a laser pump, enabling repeaterless and low cost long-haul optical transmission systems [12].

Another important achievement of the optical communication community was the development of the WDM that has enabled to highly increase the bit rate by exploring different spectral regions with wavelengths near 1.55 µm. Therefore, applying both EDFA and WDM technologies allowed the optical systems to reach the intercontinental communication. In 1996, an all optical system transmitted data at a bit rate of 5.3 Gb/s over 11 300 km of submarine cables applying 192 concatenated EDFAs spaced in 60 km [13]. Currently, there is an undersea international optical network optical interconnecting all continents and transmitting data over thousands of kilometers of optical fibers [14].

In order to increase the optical systems transmission capacity, the researchers have been studying mechanisms to obtain more communication channels. They consisted in extending the conventional WDM wavelength spectrum, known as the C-band (1.53 µm-1.57 µm), on both long and short wavelength sides creating the L and S bands. Another improvement was to decrease the channel spacing aiming to increase the operating bandwidth spectral efficiency, defining the so-called dense wavelength division multiplexing (DWDM). Moreover, Raman amplification schemes were getting attention due to their potential contribution [15]. Hence, by combining both Raman amplification and DWDM

techniques, it was demonstrated a bit rate of 10.92 Tb/s over 117 km optical fiber using 273 WDM channels, with channels spaced in 50 GHz into the L-band [16]. In the same year, another experiment got 3 Tb/s over 7380 km using 300 channels spaced in 25 GHz covering the C and L bands [17].

Coherent detection techniques, which were left aside with the rise of EDFAs in 1980s, have been playing a key role to upgrade the spectral efficiency of the WDM systems until today. Combining digital signal processing (DSP) algorithms and advanced modulation formats [18], it became to be called digital coherent detection [19], in which not only the amplitude of the electric field can be modulated, but also phase and polarization. These systems have achieved higher bit rates of 64 Tb/s [20] for example, toward the theoretical Shannon limit of spectral efficiency [21] which it is not possible to surpass using technologies based only on SMFs.

Additionally, the massive increase in internet users, networked devices, data center interconnect (DCI) applications and the rise of 5G technology combined with the advances in optical wireless communication (OWC), that should boost the Internet of Things (IoT) applications, such as smart wearables, smart homes, internet reality tools, driverless car, etc [22], may lead a capacity crunch scenario of the ongoing optical transport network [23, 24].

As a example, the Cisco Annual Internet Report [25] projects the internet will have 5.3 billion users, corresponding to 66% of global population by 2023. And the number connected devices will be 29.3 billion, corresponding to 3.6 networked devices per capita by 2023, against 2.4 networked devices per capita in 2018. In order to meet the forecasted bandwidth demand, the Space-Division Multiplexing (SDM) is the last remaining dimension in fiber communication system capable of overcoming the capacity limit of the current optical networks [26]. A SDM system makes use of multiple spacial channels exploring other available degrees of freedom when multi-core fibers (MCFs) and few-mode fibers (FMFs) are employed so a single fiber capacity could be increased by folds [27].

The first idea of using SDM dates back to 1979, when researchers made a single fiber with multiple cores, known as MCF [28]. The alternative approach, in which different optical modes define spatial channels within a MMF, dates back to 1982 [29]. However, only in recent years SDM have received serious attention to be the most promising approach to further increase fiber data transmission capacity beyond the single-mode limit [21] by tapping into the spatial diversity of MCFs and FMFs to multiply the transmission capacity of the optical systems [30, 31].

As a result, the FMFs, the focus of study of this work, open a possibility for SDM systems implementation, among the ones listed in this chapter. FMF is an optical device able to carry information exploring different transverse modes for light propagation, thus it plays a central role in application of the mode-division multiplexing (MDM) [32]. In

contrast to a conventional MMF, capable of guiding tens to hundreds of modes, a FMF has a particular geometry to provide control of propagating modes so that only a few higher-order modes (HOMs) are guided as well the fundamental mode. In general, the refractive index contrast of those fibers is small so the weakly guiding approximation is satisfied and the supported modes are referred as linearly polarized (LP) modes [33]. Overall, its core area is larger than SMF and the refractive index distribution has a parabolic profile, like a graded-index fiber. Its intermodal crosstalk is limited, since only a few modes are propagating, enabling multiple-input multiple-output (MIMO) decoding [34].

In the last ten years, many reports have demonstrated transmission systems based on MDM through FMFs links [35–40], with each mode being used as an independent data channel and MIMO techniques applied to reverse the modes overlapping issue. To highlight some of them, in 2012, three spatial modes over two different polarization were used as a channel to transmit simultaneously 240 Gb/s over 96 km of FMF [35]. The evolution of this technology was fast enough so that only five years later another experiment demonstrated the transmission of 138 Tb/s over 650 km of FMF using six spatial modes over two polarizations [36]. In 2020, a weakly-coupled MDM system employed ten spatial modes with dual polarization, totaling twenty modes used as data channels [40].

Another technology belonging optical systems is the Silicon Photonics (SiPh). Its potential was recognized still in 1980s, when researches reported the optical guiding on a single crystal silicon [41] as well as the tight optical confinement obtained when crystalline silicon (Si) is surrounded by lower index claddings, such as silicon dioxide (SiO_2) giving rise to the Silicon-On-Insulator (SOI) wafer [42, 43]. That is a useful structure to build photonic integrated circuits (PICs) for operation at telecommunication wavelengths.

Moreover, one of SiPh main advantages is its compatibility with complementary metal-oxide semiconductor (CMOS) technology fabrication process, resulting in high-volume production at low cost. Furthermore, integrated optics could achieve high data densities and transmission over longer distances with lower power consumption [44]. As a result, the suitable integration with microelectronics as well as the cost and power efficiencies provided by SiPh, makes it a key solution of miniaturizing optical devices for the next generation of the optical communication systems [45].

Following the development of transmission over optical fibers, the PICs, capable of operating MDM systems have been widely investigated, such as multimode waveguides and low inter-modal crosstalk bends [46, 47], junctions [48], directional couplers and microring resonators [49], efficient grating couplers [50, 51], (de)multiplexers [52–54], etc. Recently, an article has integrated WDM, MDM and SiPh technologies to demonstrate a 4.36 Tb/s transmission link over a FMF [55]. In this experiment, a PIC built in a SOI platform was used to excite different transverse modes and couple them into the FMF to be used as independent data channels.

1.2 Mode characterization

A key step towards the development of more complex and efficient multimode devices is the characterization technique employed in order to understand the behavior of propagating modes. Hence, distinct methods for modal content characterization have been explored in the literature. Among them, one technique consists in evaluating the laser by its beam quality factor, M^2 [56], with highest values assumed to be a few higher or equal to one. In that case, the beam is considerable stable and equivalent to single-mode propagation condition.

However, as the output power of fiber lasers increases, nonlinear processes become a limiting factor and, consequently, a large-mode-area (LMA) fiber, can be used to mitigate this problem [57, 58]. On the other hand, the higher effective area allows the propagation of HOMs, degrading the output beam quality and the evaluation of M^2 parameter should be done in the presence of several modes [59].

This analysis is not always efficient because, in some situations, even though the measured M^2 values are low and close to one, meaning single-mode operation and thus a good beam quality, there is a large amount of power distributed in HOMs [60]. This results in modal interference which causes beam fluctuations so the output beam is actually degraded. Therefore, M^2 parameter evaluation is good mainly for single mode operation. Furthermore, this technique does not provide information about the phases of the excited modes.

In order to improve the characterization of optical fibers and assess its applicability at MDM systems, Shapira *et al.* [61] have demonstrated the first complete modal decomposition method based on a phase retrieval algorithm. This technique enables the acquisition of the propagating modes characteristics, both intensity and phase. However, it requires a prior knowledge of the field distribution of the fiber under test (FUT) optical modes.

To overcome this limitation, some methods apply the Fourier optics as a tool for modal decomposition. Some of them are based on optical correlation analysis [62, 63] and apply holographic optical elements (HOEs) to measure the intermodal weights and phases of the supported modes by a MMF. Other techniques apply optical reflectometry [64, 65] to measure the differential mode delay and the power coupling between the modes. However, these techniques are not able to retrieve profile information data from each mode.

The scientific community's efforts to develop methods capable to perform a complete modal discrimination of waveguides, optical fibers in particular, including field profile information of each mode, from a direct experimental measurement of modal content without needing previous knowledge of its eigenmodes led to new measurement techniques. These techniques are based on the principle that non-degenerate fiber modes travel at different group velocity along the fiber length.

A well-known method that relies on this principle is the Cross-correlated Imaging (C^2) [66]. It works using an optical low-coherence interferometry and its analysis is performed from the interference between an external reference arm beam and the fiber output that contains the information about the modes excited in the FUT. After, modal profiles, group delays, dispersion and their relative weights can be obtained for all supported modes. Nevertheless, alike all methods listed so far, it requires interferometric techniques on its experimental setup.

Multi-Path Interference (MPI) is a well-known phenomenon caused by the beating between the signals and their weak replicas that strongly degrade the performance of the optical communications systems [67]. In FMFs, as a consequence of fiber modes travelling at different group velocities, the coherent MPI is caused by the beating of signals as a result of the group delays of the modes and can lead to a slow time-scale power fluctuations [68]. In order to measure and extract information from these oscillations, Nicholson *et al.* [68, 69] have proposed the Spatially and Spectrally Resolved Imaging (S^2), a method for modal content characterization in LMA fibers.

The S^2 allows to identify the excited modes in the fiber and determine their optical power and relative phases by a direct measurement of the spectral interference pattern generated by the spatial beating between the propagating modes. The S^2 is interferometrically based on the fundamental mode propagating through the FUT at the probe arm, so an external reference arm is not necessary.

In addition to characterize different types and MPI levels of the modes, the method could also measure beam instabilities caused by fluctuating phases between the modes. As a drawback, it was only applied to LMA fibers because the large core makes it feasible to move a SMF probe in both perpendicular axes to the beam propagation direction coming from the FUT. This process aims to make a two-dimensional scanning at every position, x and y, of the output surface of the LMA fiber.

The scanning is time consuming what hinders the excitation and measurement of HOMs because they are sensitive to disturbances in the experiment. With the goal of speeding up this process, Nguyen *et al.* [70] have proposed a change to the conventional S^2 method that consists in replacing the two-dimensional spatial scanning by the one-dimensional wavelength scanning. As a result, the experiment becomes much faster, it is not limited to LMAs fibers and there is no moving part at the FUT output, thus the optical alignment is straightforward.

Furthermore, the conventional S^2 method does not take in consideration the spectral interferences generated by the spatial beating between two HOMs. It assumes the power of these modes are low, so the beating contribution can be neglected. However, this is not always valid because the beating between HOMs can occur, and its relative power can be considerable in comparison of a beating between the fundamental mode and one HOM. Therefore, all contributions should be counted [70], and the mathematical

description that considers all terms will be presented in chapter 2.

Applying the aforementioned improvements to the S^2 method, a hollow-core photonic crystal fiber (HC-PCF) was characterized by Lamilla Rubio [71]. In order to also recover the highly-dispersive surface modes supported by the FUT, an external free-space arm with the fundamental mode was added to the experimental setup. This was needed because the highly-dispersive modes only interacted with the fundamental mode in a region in the middle of the transmission spectrum where the fundamental mode was strongly attenuated. Since the fundamental mode was not dominant, the characterization results via S^2 method was not precise and the addition of the reference arm aforementioned was the solution found. As a result, this modification has enabled a more complete characterization of the fiber analyzed [72].

In this work, the S^2 method is applied with one-dimensional scanning of the wavelength. The FUT is a FMF developed by Corning Incorporated. Unlike the HC-PCF that supports surface modes, the FMF only supports weakly-guiding modes. Therefore, a complete discrimination of modal content is demonstrated with no need for an external reference arm. All transverse modes supported by the FMF under test are recovered. The group delay value and modal profile including intensity distribution and relative phase of each mode are presented. To better interpret and validate the achieved results, an approximate geometry of the fiber is simulated using Finite Element Method (FEM) to calculate its propagating content.

Furthermore, after developing the know-how for modal content characterization in optical fibers, the method is employed to characterize an integrated multimode coupler for FMFs that was developed by Applied and Computational Electromagnetics Group (GEMAC). In the literature, this is the first application of S^2 method for modal content discrimination of integrated couplers, which could pave the way for the development of more complex integrated multimode devices that are useful for MDM applications and thus require a more precise characterization.

1.3 Objectives

In the interest of clarifying the central idea of this work, our objectives are to:

- explain the principle of operation by a theoretical and mathematical discussion of the S^2 method as well as the particularities of its experimental implementation;
- perform the modal content characterization of the FMF under test by applying the studied method;
- validate the experimental results by executing the mode analysis of the FUT;

- perform the characterization of the fiber when excited by a silicon integrated tri-modal coupler, demonstrating the decomposition of its modal content and validating its operation.

1.4 Work organization

This document is organized in five chapters. The Chapter 1 is the Introduction, where an overview of the optical systems is presented, since the first multimode system operating in the wavelength region near 0.8 µm, covering the advent of WDM and EDFA, until the most advanced systems that employ different techniques to achieve high bit rates and the ones employing the SiPh technology. Chapter 2 presents the explanation about the S^2 method principle of operation of according to the improvement mentioned in section 1.2 and the implementation of the experimental setup. The achieved results from the FMF under test characterization, as well as its validation are presented and discussed in Chapter 3. Chapter 4 demonstrates the implementation of S^2 method to recover the modal content of the FMF under test when excited by a silicon integrated tri-modal coupler in order to validate the proper operation of the device. Finally, in Chapter 5, there are the final considerations and future perspectives for this work.

Chapter 2

Spatially and Spectrally Resolved Imaging Method

As mentioned in section 1.2, the S^2 method is one that relies on the principle that the fiber modes propagate at different group velocities, what creates spectral interferences due to the group delay between the fundamental mode, the fastest mode, and the HOMs, that travel at slower velocities. Thus, the measurements of differential group delay (DGD) reveal the modal content. In addition to measure relative optical power of transverse modes, similar to methods previously cited [64,65], this technique also allows the extraction of the modal profiles, intensity and relative phase, of each mode.

The description of S^2 method proposed by Nicholson *et al.* [68] only considers the interference between the fundamental mode and HOMs, because it assumes the power of HOMs is too low compared to the power of fundamental mode, and the interference between two HOMs could be then neglected. This simplification is valid for several cases, but it is not the most generalized approach. So, as an improvement, Nguyen *et al.* [70] demonstrated theoretically that the interference between HOMs always appear in the S^2 technique when the FUT supports two or more HOMs. Therefore, the algorithm used to perform the technique calculation should consider all those kinds of interferences.

The presence of different transverse modes into a optical fiber generates spectral interferences due to the propagation delay between the HOMs and the fundamental mode. The S^2 imaging technique executes the measurement of these interferences observed in the near-field images captured at the output of the FUT, and then the processing of the spectrally and spatially solved interference images.

The images contains information of the beam shape captured at the output of the FUT for different wavelength values. One then can measure the optical spectrum at a single pixel of the set of images as presented in fig. 2.1a. It is possible to see an interference pattern due to the presence of modes, which are more clearly observed in the Fourier transform of the spectrum, fig. 2.1b, where the spectral interferences lead to different mode beats at different time delays, represented by the peaks on the curve. The

peaks are the beating mode of many modes supported by the fiber.

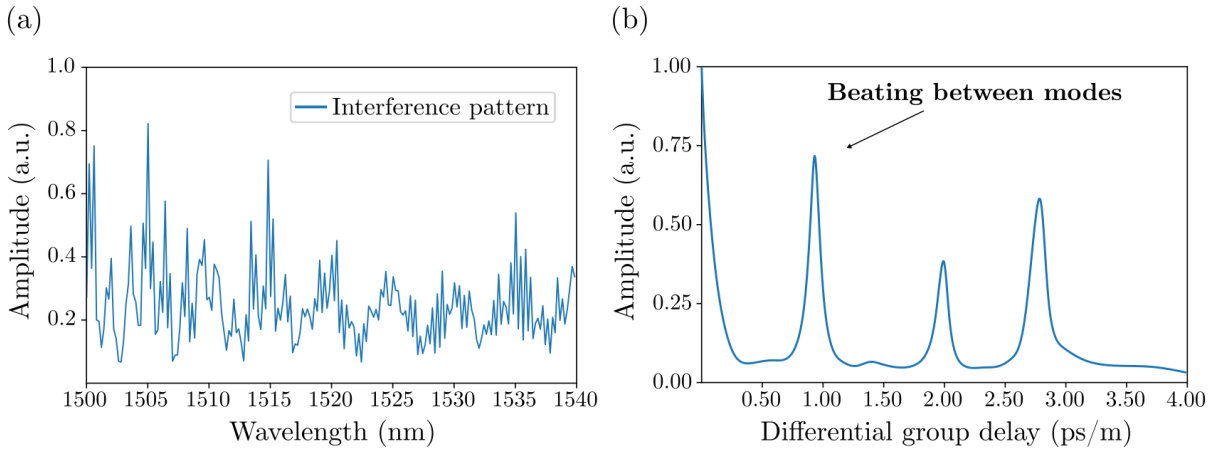

Figure 2.1: (a) Optical spectrum measured at a single pixel and its Fourier transform in (b), where the peaks occur as a result of beating between the modes.

2.1 Theoretical discussion

This section presents the mathematical basis of the algorithm to perform the S^2 method, according Nguyen *et al.* [70]. Additionally, an explanation about the principle of operation of the S^2 method will be also presented. First consider that the output of a light source is launched into the optical fiber input and the electric field at the fiber output, $\mathbf{E}_{out}(x, y, \omega)$, is given as the superposition of the propagating modes through the waveguide.

$$\mathbf{E}_{out}(x, y, \omega) = \sum_{j=0}^{n} \mathbf{E}_j(x, y, \omega). \tag{2.1}$$

The quantity $\mathbf{E}_j(x, y, \omega)$ represents the electric field of different propagating modes for a fiber that supports $n + 1$ modes. The amplitude of the fundamental mode is represented by $E_0(x, y, \omega)$, that will be used as reference due to its power level, field distribution profile and propagation on the fast axis of the fiber. The amplitude of each mode can be related to the amplitude of fundamental mode by a constant *alpha*, $\alpha(x, y)$, that is weakly dependent on λ considering a small wavelength window.

$$E_j(x, y, \omega) = \alpha_j(x, y) E_0(x, y, \omega) e^{i\omega\tau_j}. \tag{2.2}$$

Where τ_j is the period of the beat frequency between the corresponding HOM and the fundamental mode. Since the fundamental mode is the reference, $\tau_0 = 0$ and thus

$\alpha_0(x,y) = 1$. Now, taking the squared modulus of the output electric field:

$$|E_{out}(x,y,\omega)|^2 = |E_0(x,y,\omega)|^2 \left|\sum_{j=0}^{n} \alpha_j(x,y) e^{i\omega\tau_j}\right|^2$$
$$= |E_0(x,y,\omega)|^2 \left[\sum_{j=0}^{n}\sum_{k=0}^{n} \alpha_j(x,y)\alpha_k^*(x,y) e^{i\omega(\tau_j-\tau_k)}\right]. \quad (2.3)$$

The terms in the double summation can be separated into:

1. For $j = 0$, $k = 0 \Rightarrow \alpha_0.\alpha_0^*.e^{i\omega(\tau_0-\tau_0)} = |\alpha_0|^2 e^0 = 1$;
2. For $j = 0$, $k \neq 0 \Rightarrow \sum_{k=1}^{n} \alpha_0\alpha_k^* e^{i\omega(\tau_0-\tau_k)} = \sum_{k=1}^{n} \alpha_0\alpha_k^* e^{-i\omega\tau_k}$;
3. For $j \neq 0$, $k = 0 \Rightarrow \sum_{j=1}^{n} \alpha_j\alpha_0^* e^{i\omega(\tau_j-\tau_0)} = \sum_{j=1}^{n} \alpha_j\alpha_0^* e^{i\omega\tau_j}$;
4. For $j \neq 0$, $k \neq 0$ and $j = k \Rightarrow \sum_{j=1}^{n}\sum_{k=j}^{n} \alpha_j\alpha_j^* e^{i\omega(\tau_j-\tau_j)} = \sum_{j=1}^{n} |\alpha_j|^2$;
5. For $j \neq 0$, $k \neq 0$ and $j \neq k \Rightarrow \sum_{j=1}^{n-1}\sum_{k=j+1}^{n} \left[\alpha_j\alpha_k^* e^{i\omega(\tau_j-\tau_k)} + \alpha_k\alpha_j^* e^{i\omega(\tau_k-\tau_j)}\right] = \sum_{j=1}^{n-1}\sum_{k=j+1}^{n} 2\mathbb{R}\{\alpha_j\alpha_k^* e^{i\omega(\tau_j-\tau_k)}\}$.

Note the terms in 3 are the complex conjugate of those in 2. Substituting all terms in (2.3) and considering the optical intensity, $I_{out}(x,y,\omega)$, is proportional to $|E_{out}(x,y,\omega)|^2$, it follows that:

$$I_{out}(x,y,\omega) = I_0(x,y,\omega)\left[1 + \sum_{j=1}^{n}|\alpha_j|^2 + \sum_{j=1}^{n} 2\mathbb{R}\{\alpha_j e^{i\omega\tau_j}\} + \sum_{j=1}^{n-1}\sum_{k=j+1}^{n} 2\mathbb{R}\{\alpha_j\alpha_k^* e^{i\omega(\tau_j-\tau_k)}\}\right]$$
$$= I_0(x,y,\omega)\left[1 + \sum_{j=1}^{n}|\alpha_j|^2 + \sum_{j=1}^{n} 2\,|\alpha_j(x,y)|\, cos(\omega\tau_j + \theta_j) + \right.$$
$$\left. \sum_{j=1}^{n-1}\sum_{k=j+1}^{n} 2\,|\alpha_j(x,y)|\,|\alpha_k(x,y)|\, cos(\omega\tau_j + \theta_j - \omega\tau_k - \theta_k)\right]. \quad (2.4)$$

Where $I_0(x,y,\omega)$ is the optical intensity distribution of the fundamental mode. The first and the second terms inside the brackets represent the sum of optical intensities of all propagating modes. In the third term, τ_j is the period of the beat frequency between the fundamental mode and HOMs and thus this term represents the sum of spectral interference patterns due to the DGD between *j-th* HOMs and the fundamental mode.

Finally, the last term represents the sum of spectral interference patterns caused by the DGD between two HOMs, one represented by j and the other by k, so τ_k is similar to τ_j and it is used to refer to the other HOM. The parameters θ_j and θ_k in cosine arguments represent the relative phases of the correspondings HOMs with respect to the fundamental mode.

The Inverse Fourier Transform (IFT) of the optical intensity is calculated by:

$$\begin{aligned}\tilde{I}_{out}(x,y,\tau) &= \mathscr{F}^{-1}\{I_{out}(x,y,\omega)\} = \frac{1}{2\pi}\int_{-\infty}^{\infty} I_{out}(x,y,\omega)e^{i\omega\tau}d\omega \\ &= \frac{1}{2\pi}\left\{\int_{-\infty}^{\infty} I_0(x,y,\omega)e^{i\omega\tau}d\omega + \int_{-\infty}^{\infty}\sum_{j=1}^{n}|\alpha_j|^2 I_0(x,y,\omega)e^{i\omega\tau}d\omega\right. \\ &+ \int_{-\infty}^{\infty}\sum_{j=1}^{n}|\alpha_j| I_0(x,y,\omega)\left[e^{i(\theta_j+\omega\tau_j)} + e^{-i(\theta_j+\omega\tau_j)}\right]e^{i\omega\tau}d\omega \\ &+ \int_{-\infty}^{\infty}\sum_{j=1}^{n-1}\sum_{k=j+1}^{n}|\alpha_j||\alpha_k| I_0(x,y,\omega)\left[e^{i(\theta_j-\theta_k+\omega\tau_j-\omega\tau_k)}\right. \\ &\qquad\left.\left. + e^{-i(\theta_j-\theta_k+\omega\tau_j-\omega\tau_k)}\right]e^{i\omega\tau}d\omega\right\}.\end{aligned} \tag{2.5}$$

Therefore,

$$\begin{aligned}\tilde{I}_{out}(x,y,\tau) &= \tilde{I}_0(x,y,\tau)\left[1+\sum_{j=1}^{n}|\alpha_j(x,y)|^2\right] + \sum_{j=1}^{n}\alpha_j(x,y)\tilde{I}_0(x,y,\tau+\tau_j) \\ &+ \sum_{j=1}^{n}\alpha_j^*(x,y)\tilde{I}_0(x,y,\tau-\tau_j) + \sum_{j=1}^{n-1}\sum_{k=j+1}^{n}\alpha_j(x,y)\alpha_k^*(x,y)\tilde{I}_0(x,y,\tau+\tau_j-\tau_k) \\ &+ \sum_{j=1}^{n-1}\sum_{k=j+1}^{n}\alpha_j^*(x,y)\alpha_k(x,y)\tilde{I}_0(x,y,\tau-(\tau_j-\tau_k)),\end{aligned} \tag{2.6}$$

in which $\tilde{I}_0(x,y,\tau)$ represents the IFT of the optical intensity of the fundamental mode.

From (2.6), it is possible to find the time domain spectral intensity at different values of τ and therefore to establish a relation between the amplitudes of the fundamental mode and the propagating HOMs. The amplitude ratio, defined as $f_j(x,y)$, is generated by the interference between the corresponding HOM and the fundamental mode, and it can be calculated as the time domain spectral intensity at the DGD of interest divided by the time domain spectral intensity at group delay zero, as follow.

$$f_j(x,y) = \frac{\tilde{I}_{out}(x,y,\tau=\tau_j)}{\tilde{I}_{out}(x,y,\tau=0)} = \frac{\alpha_j^*(x,y)}{1+\sum_{j=1}^{n}|\alpha_j(x,y)|^2} \tag{2.7}$$

Similarly, it is possible to define the amplitude ratio, $f_{jk}(x,y)$, due to the interferences between HOMs at the time delay $|\tau_j-\tau_k|$, and it can be calculated as:

$$f_{jk}(x,y) = \frac{\tilde{I}_{out}(x,y,\tau=\tau_j-\tau_k)}{\tilde{I}_{out}(x,y,\tau=0)} = \frac{\alpha_j^*(x,y)\alpha_k(x,y)}{1+\sum_{j=1}^{n}|\alpha_j(x,y)|^2} \tag{2.8}$$

The spectral interferences between propagating modes lead to peaks in the Fourier transform of the optical spectrum as previously shown in fig. 2.1. The peaks

generated as a result of the beating between *j-th* HOMs and the fundamental mode have the modal content of the optical modes that are propagating in the fiber. The peaks generated by the beating between two HOMs can be named as spurious peaks. The appearance of these last peaks in Fourier transform of the optical spectrum is not desirable, but since can appear it is necessary to understand that the recovered information represent a beating between two HOMs propagating in the FUT. In Chapter 3, we will observe this kind of peak in the experimental results.

Following the mathematical development, from (2.7) it is possible to find an equation to calculate the value α that relates the amplitudes of the HOMs and the fundamental mode. The value α for each HOM will be used to recover its modal profile. The equation for $\alpha_j(x, y)$ is:

$$\alpha_j^*(x,y) = f_j(x,y)\left(1 + \sum_{j=1}^{n} |\alpha_j(x,y)|^2\right) \tag{2.9}$$

To isolate α_j, we take the squared modulus and apply the summation, such as:

$$\sum_{j=1}^{n} |\alpha_j|^2 = \sum_{j=1}^{n} |f_j|^2 \left|1 + \sum_{i=1}^{n} |\alpha_i|^2\right|^2$$

If $x = 1 + \sum_{i=1}^{n} |\alpha_i|^2$, it implies that:

$$\begin{aligned} x - 1 &= \sum_{j=1}^{n} |f_j|^2 x^2 \\ \sum_{j=1}^{n} |f_j|^2 x^2 - x + 1 &= 0 \\ x &= \frac{1 \pm \sqrt{1 - 4\sum_{j=1}^{n} |f_j|^2}}{2\sum_{j=1}^{n} |f_j|^2} \end{aligned} \tag{2.10}$$

Combining (2.9) and (2.10):

$$\alpha_j^*(x,y) = f_j(x,y)\left[\frac{1 \pm \sqrt{1 - 4\sum_{j=1}^{n} |f_j(x,y)|^2}}{2\sum_{j=1}^{n} |f_j(x,y)|^2}\right] \tag{2.11}$$

Finally, it is possible to evaluate both the optical intensity of the fundamental mode, $\tilde{I}_0(x, y)$, and the optical intensity of the HOM at the DGD of interest, $\tilde{I}_j(x, y, \tau_j)$, as follows [68]:

$$\tilde{I}_0(x,y) = \tilde{I}_{out}(x,y,\tau=0)\left[\frac{1}{1 + \sum_{j=1}^{n} |\alpha_j(x,y)|^2}\right] \tag{2.12}$$

$$\tilde{I}_j(x,y,\tau_j) = \tilde{I}_{out}(x,y,\tau=0)\left[\frac{|\alpha_j(x,y)|^2}{1+\sum_{j=1}^{n}|\alpha_j(x,y)|^2}\right] \tag{2.13}$$

2.2 Experimental implementation

In this work, the experimental setup follows the approach proposed by Nguyen *et al.* [70], in which a tunable laser source (TLS) and an InGaAs camera are used to perform an one-dimensional scanning of the wavelength. The other approach employs a broadband source, instead of the TLS, a 2-axis scanning stage and an optical spectrum analyzer (OSA), instead of the camera, to perform a two-dimensional scanning at every position of the output surface of the fiber [68, 71]. The first implementation has the advantages of accelerating the measurement process, it is not limited to a specific type of optical fiber and the optical alignment at the FUT output is straightforward. Figure 2.2 shows the scheme of the experimental setup to execute the modal characterization of the FMF under analysis developed by Corning.

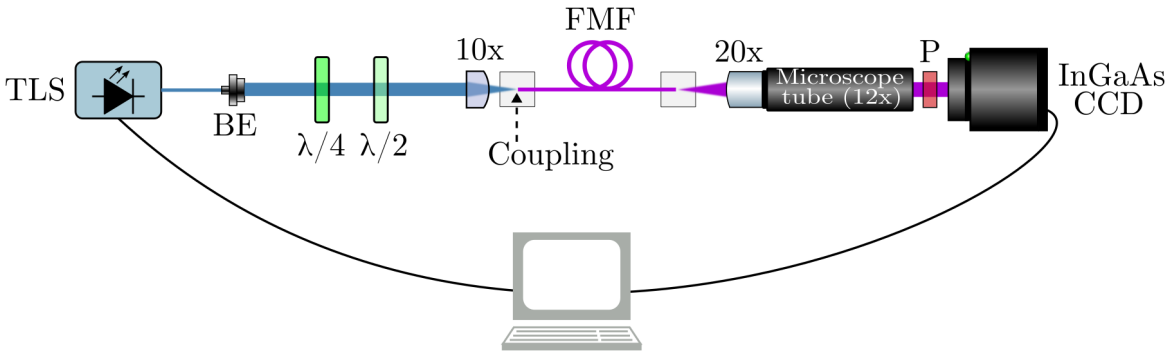

Figure 2.2: Scheme of the experimental setup.

The TLS is set to perform a continuous sweep inside a pre-defined wavelength window at a speed of 0.5 nm/s, which results in a wavelength step of about 10 pm. The coming light from the source passes through a beam expander (BE) and the resulting collimated beam is filtered by the $\lambda/4$ and $\lambda/2$ waveplates, where the appropriate polarization is reached to ensure that only one state of polarization (SoP) of the fundamental mode is excited in the FMF.

The beam then passes through a 10× objective lens, with 5.5 mm working distance, to be focused into the FMF input, that is positioned on a 3-axis optical alignment stage. The fiber output beam is magnified by a 20× objective lens, with 20 mm working distance, connected to a 12× microscope tube. The magnified beam passes through a linear polarizer (P) to filter rotated versions of the output electric field, that can occur as a result of fiber birefringence. Finally, the near-field images are captured by the InGaAs camera and the information is recorded by the computer.

2.2.1 Data acquisition and post-processing steps

The data acquisition process is performed by means of an one-dimensional scanning of the laser source wavelength. While the wavelength of the TLS is swept across a pre-defined window, the incoming light beam from the FMF is captured by the camera. One image is recorded for each wavelength set by the TLS. The recorded data are then post-processed to calculate the IFT curve and recover the modal profiles and relative phases according to section 2.1.

The data acquisition and post-processing steps are illustrated by fig. 2.3. The images are captured by the camera and recorded as two-dimensional pixels matrices, where x and y axes are the columns and rows of each matrix. The beam profiles are not symmetric: the complex shape is due to the interference between different modes supported by the fiber. While the laser source wavelength is scanned, the captured images are recorded for each wavelength, thus composing the third axis of the matrix data that will be post-processed.

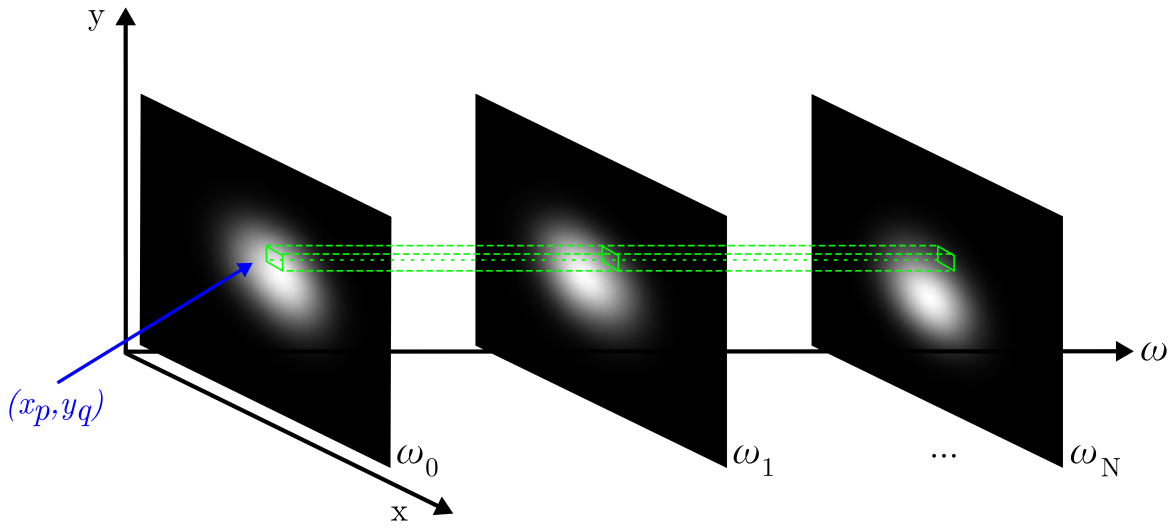

Figure 2.3: Representation of the three-dimensional matrix data obtained during measurement used to perform the IFT computation process for S^2.

Since the scanning continuous, the wavelength values for each captured image are not necessarily equally spaced. The scan could be done with equally spaced wavelengths, but this would take much longer time, which is adverse to the measurement process, because since excitation of HOMs is very sensitive to any disturbance, the longer it takes, the worse the measurement becomes. In order to overcome this issue is used the continuous sweep, that is faster. Then, the wavelength values are interpolated in order to obtain an uniform grid in this third axis of the matrix data. After it, the post-processing algorithm performs the IFT calculation. The transformation is calculated at each given coordinate pixel, denoted as (x_p, y_p) in fig. 2.3, for all images along the interpolated frequency axis.

After performing the IFT calculation, the three-dimensional matrix of interest,

$\tilde{I}_{out}(x, y, \tau)$, is obtained. It contains information about optical intensity for all propagating modes in the time domain. From that, it is possible to determine the IFT of the spectral intensity for different values of group delay τ and establish the amplitude ratio, $f(x, y)$, to calculate the constant *alpha*, $\alpha(x, y)$, for each group delay value where occurs a spectral interference between the propagating modes, also called as beating tone. The beating tones are recognized as peaks in the IFT curve. This curve is calculated from the three-dimensional matrix of interest, as the average of absolute values of all pixels from each image.

$$P_{avg}(\tau) = \iint \left|\tilde{I}_{out}(x, y, \tau)\right| dxdy \tag{2.14}$$

Thus, the plot of P_{avg} versus τ, illustrated in fig. 2.4, allows to identify peaks that represent the beatings between different fiber modes. The mode recovery should be executed for the DGD corresponding to each peak to recover the modal content. In fig. 2.4 only one HOM is represented. More peaks would appear if two or more HOMs are excited in the experiment, some of them can be a beating between the fundamental mode and one HOM as well as it can be a beating between two HOMs.

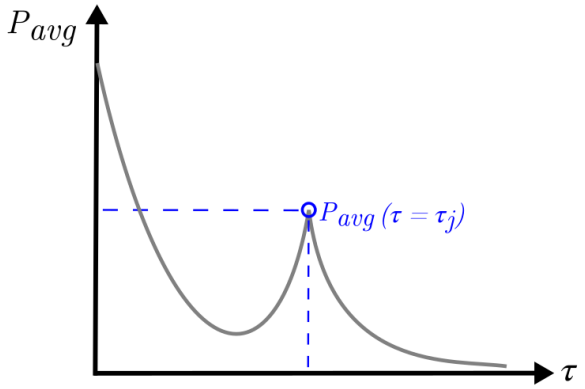

Figure 2.4: The typical IFT curve of the optical spectrum. In general, the average optical power (y-axis) is normalized in dB and the DGD (x-axis) is normalized in ps/m.

After the identification of the peaks in the IFT curve, the algorithm executes the mode recovery according to the equations shown in section 2.1, so that the electric field is calculated from the optical intensity and α at the DGD of interest. Finally, it possible to obtain the mode profile, intensities and relative phases of the propagating modes.

In fig. 2.5, the tasks executed are presented in a steps diagram for the S^2 method implementation. The data acquisition step is the measurement process. All the next tasks are part of the post-processing and they are executed by the S^2 algorithm. The one-dimensional and three-dimensional matrices resulted at the end of each task are also shown in the diagram.

The experimental data is organized in the $I_{out}(x, y, \lambda)$ matrix after the mea-

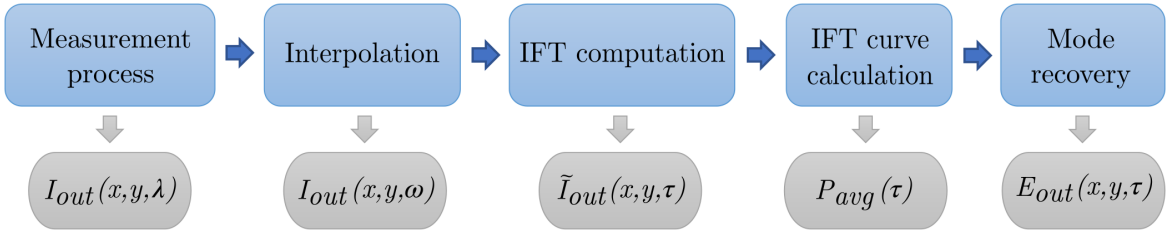

Figure 2.5: Diagram of the steps executed for the S^2 method implementation.

surement process ends. It contains information about the spatial beating pattern captured by the camera. Therefore, the interpolation of the data is performed to obtain a frequency uniform grid, thus resulting in the $I_{out}(x, y, \omega)$ matrix. The IFT is then calculated to obtain the matrix of interest, $\tilde{I}_{out}(x, y, \tau)$, which contains information about the optical intensities in the time domain.

After then, the average of absolute values of all pixels from each image is calculated to produce the $P_{avg}(\tau)$ function, and the IFT curve is plotted. After the identification of peaks on the curve, the output electric field is calculated for the DGD values (τ) corresponding to identified peaks, thus resulting in the $E_{out}(x, y, \tau)$ matrix. The squared modulus and the phase of $E_{out}(x, y, \tau)$ are, respectively, the optical intensity and the relative phase of the modes in comparison of the reference, the fundamental mode.

2.2.2 Experimental limitations

S^2 method is an advantageous and powerful tool because it performs modal content characterization by a direct measurement of the spectral interference pattern generated due to the beating between the propagating modes with no assumption about the FUT and no necessity of previous knowledge of its eigenmodes. On the other hand, this method has some limitations that will be explained in this section.

The first limitation is due to the computational memory consumption. The experimental data contains about 2000 images of 512 × 640 pixels each, for a typical measurement with wavelength window of 40 nm in steps of about 10 pm. Thus resulting in a large three-dimensional matrix that even gets bigger when the wavelength window is increased to improve the temporal resolution after the IFT calculation. For our computer, this wavelength window could be at most 80 nm.

Another limitation is related to the signal sampling frequency that arises from the fact that the frequency domain experimental measurements are reconstructed in the time domain by applying the IFT. Since the experimental signal is band-limited according to the wavelength window set on the laser source, reconstruction of this signal will be exact if the Nyquist criteria is attended.

Since the DGD of the propagating modes is directly proportional to the fiber length, the beating frequency, in which a spectral interference occurs between the prop-

agating modes, will be determined by the signal bandwidth, the source sweep step and the fiber length too. Keeping both laser parameters fixed, the peaks in the IFT curve, called beating tones, will be resolved by the fiber length chosen according the Nyquist limit. Thus, it necessary to choose the proper fiber length for a signal reconstruction with no loss of information.

Figure 2.6 shows two possible situations for different fiber lengths while the signal bandwidth and the source sweep steep remains fixed, a wavelength step of about 10 pm which gives a frequency step of about 1 GHz. It was observed that for about 2 m of the FMF under analysis, the sampling rate of the signal was enough to satisfy the sampling theorem, with a beating frequency ($\Delta v = 1/\tau_{max}$) of about 2.6 GHz, thus resulting in a well-defined peak in the IFT curve, as shown in fig. 2.6a, after the transform calculation.

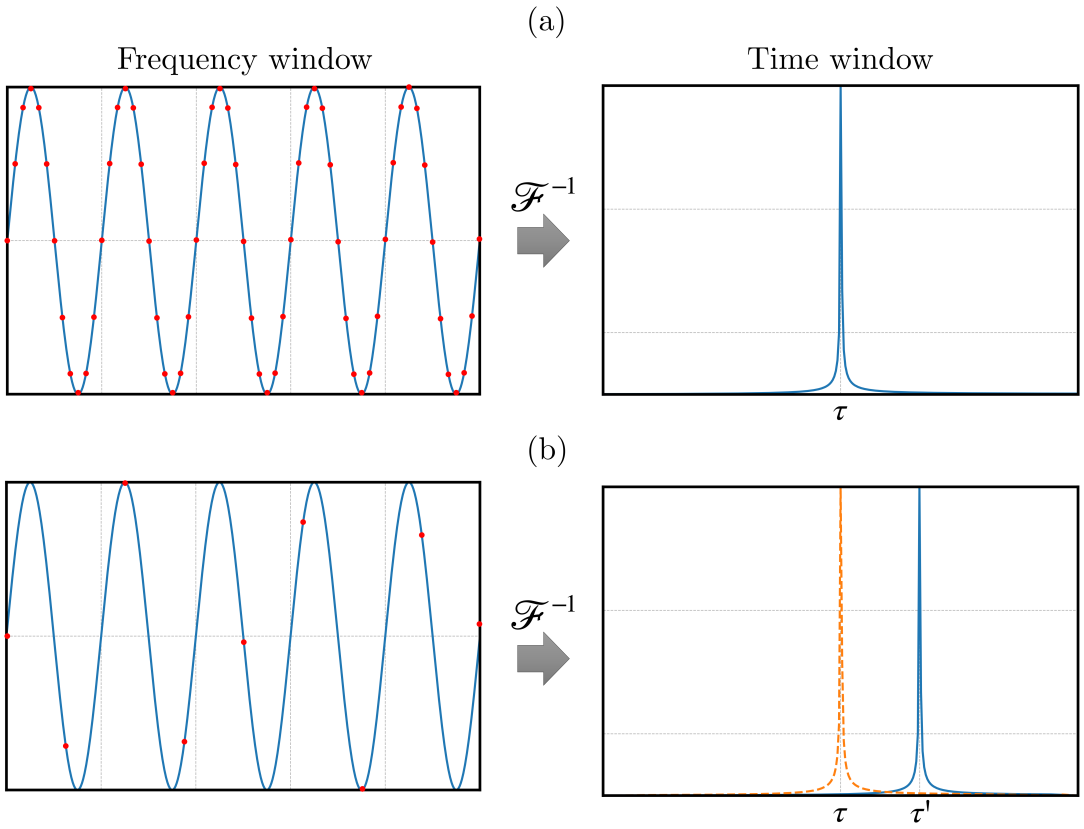

Figure 2.6: Influence of the FUT length as respect of sampling rate. (a) Representation of an ideal experimental condition. (b) Aliasing effect resulting from an inappropriate experimental condition.

On the other hand, for long fiber samples, around hundreds of meters, the sampling rate was not enough to satisfy the sampling theorem because the points per cycle were insufficient to reconstruct the optical signal, thus generating aliasing. Therefore, the peak in the IFT curve was not located at the correct position τ, but at the wrong position $\tau^{'}$ on the time window, as shown in fig. 2.6b.

Another limitation is related to the temporal resolution, that relies on how

accurate the DGD value of a specific peak on the IFT curve is. The resolution in the time window can be a problem when the fiber length is short, a few centimeters, or when two propagating modes have DGD values very close to each other. For short fibers, the peak on the IFT curve can be wide and poorly defined, thus making it impossible to determine the group delay precisely. This can be managed by increasing the wavelength window set on the laser if there is computational memory available and $\alpha(x, y)$ remains λ-independent.

The temporal resolution can also be an obstacle even if the fiber length is suitable. Because two propagating modes in this fiber with group delay values close to each other can appear as a single peak on the IFT curve, being interpreted as a single mode. This is illustrated in fig. 2.7. The frequency window shows two signals of almost equal frequencies. When executing IFT calculation, these signals will generate two defined peaks at τ_1 and τ_2 values in time window if the temporal resolution is sufficient. However, if the temporal resolution is insufficient, it will not be possible to distinguish the signals, thus generating an only peak at $\tau^{'}$ value.

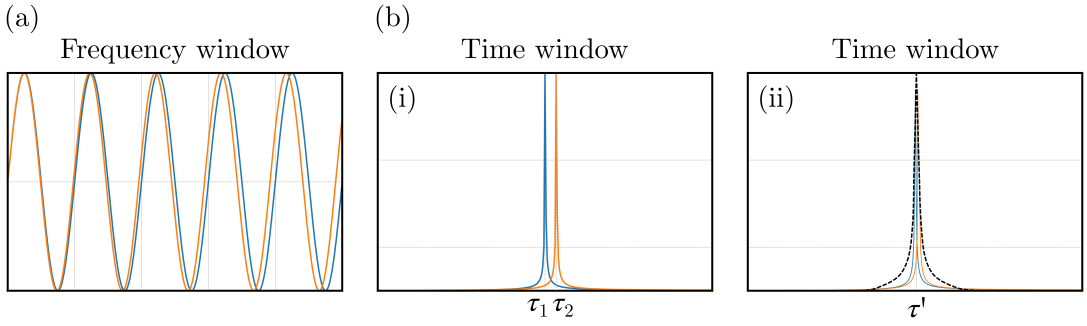

Figure 2.7: Temporal resolution in S^2 method. (a) Representation of two similar frequency signals. (b) Time window obtained after the IFT calculation, in (i) the temporal resolution is sufficient to distinguish two peaks but in (ii) does not.

The solution for this problem is to increase the signal bandwidth, by increasing the pre-defined window set on the laser, since the larger the wavelength window, the better the temporal resolution after the IFT calculation. However, in addition to the larger required memory, explained before, a large wavelength window will extend the measurement duration, increasing the experiment susceptibility to instabilities and external disturbances that affect the measured data.

Another possible route to improve the temporal resolution is to use a longer fiber, but it is necessary to be careful because the aliasing can be generated if the fiber is too long. Therefore, in order to achieve proper experimental conditions, given the limitations of the S^2 method, it is necessary to establish a correlation and dependance between the signal bandwidth, the measurement duration and the fiber sample length.

For characterization of the FMF studied in this work, two samples of about 0.9 and 1.66 m were used. The laser source was set to execute the wavelength scanning inside a window of 40 nm, that generates a temporal resolution enough to determine the correct

positions of the peaks and recover all propagating modes. Some experimental measures with larger wavelength windows of 60 nm to 80 nm (maximum computational limit of our machine) were done to obtain an even better temporal resolution. Nonetheless, as the measurements has took longer than expected, instabilities have affected the experiment negatively, thus making it impossible to recover all propagating modes specially the highly-dispersive LP_{02} mode.

Chapter 3

Few-mode fiber characterization via S^2 method

This chapter presents the results obtained from the characterization of the FMF under analysis via S^2 imaging method. We will present the experimental setup implemented, the best results achieved and an important discussion topic that it is associated to the laser source. The TLS has an intrinsic modulation of power with respect to wavelength that leads to a peak in the IFT curve. Furthermore, we present a mode analysis simulation of an approximate geometry of the FUT. The simulation is performed using FEM and it is an useful tool to better understand and interpret the experimental results.

3.1 Experimental setup and results

The experimental setup for S^2 method application was assembled in Optical Communications Laboratory (LCO) at the Photonics Research Center (Photonicamp) at UNICAMP, according to the description presented in section 2.2. Figure 3.1 illustrates the experimental S^2 setup implemented as well as the equipments and optical components used. The TLS is a Laser model Keysight from Agilent Technologies model 8164B. It has a linewidth of 10 kHz and it is set to perform a wavelength scan inside a pre-defined range from 1500 nm to 1540 nm.

The light beam from the TLS is guided by a SMF to a beam expander. The expanded and collimated beam passes through two beam attenuators that adjust the optical power to avoid the camera saturation. Then, the beam passes through the quarter and half-wave plates and it is focused into the FMF input by a 10× objective lens. The FUT sample length is 1.66 m. The fiber output beam is magnified by a 20× objective lens connected to a 12× microscope tube and passes through a linear polarizer. Finally, the beam profiles are captured by the camera. The InGaAs camera is a charge-coupled device (CCD) from Photonic Science.

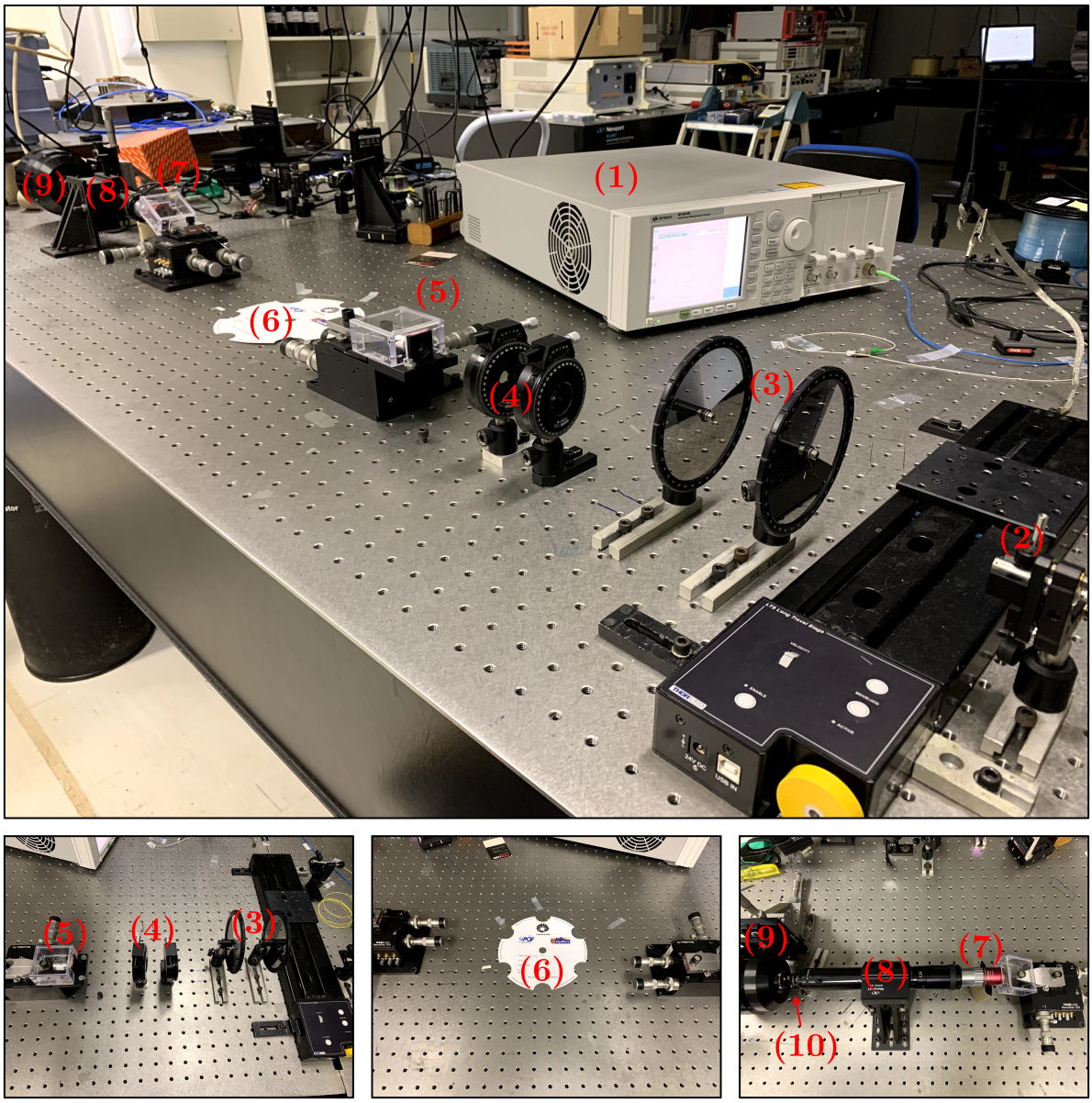

Figure 3.1: Picture of the experimental setup assembled at LCO/Photonicamp to execute the characterization of the FMF via S^2 method. (1) - Laser source (TLS), (2) - beam expander, (3) - beam attenuators, (4) - quarter and half-wave plates, (5) - 10× objetive lens, (6) - FUT sample, (7) - 20× objetive lens, (8) - 12× microscope tube, (9) - InGaAs camera and (10) - linear polarizer.

While the laser executes the wavelength scan, the magnified fiber output beam profile is detected by the camera sensor. These images are recorded for each wavelength set by the TLS during the data acquisition step. As explained in section 2.2.1, the beam profiles are not symmetric due to the interference between different modes supported by the fiber. So, the complex shape of the output beam is resulted of the modal overlap that occur while the light travels along the fiber sample.

Therefore, the images that contain information about the overlap of the modes are recorded and organized in a three-dimensional matrix, $I_{out}(x, y, \lambda)$, where the coor-

dinates (x, y) correspond to the image for each wavelength (λ) swept by the TLS. The interference pattern generated due to the propagation of different modes along the fiber can be detected in a specific pixel of all images as the wavelength is swept, as shown in fig. 3.2. This signal is proportional to the optical power at that pixel and, thus, the amplitude fluctuations arise as the supported modes interfere spectrally. The different beating periods in the interference pattern in a single pixel are due to the presence of different HOMs.

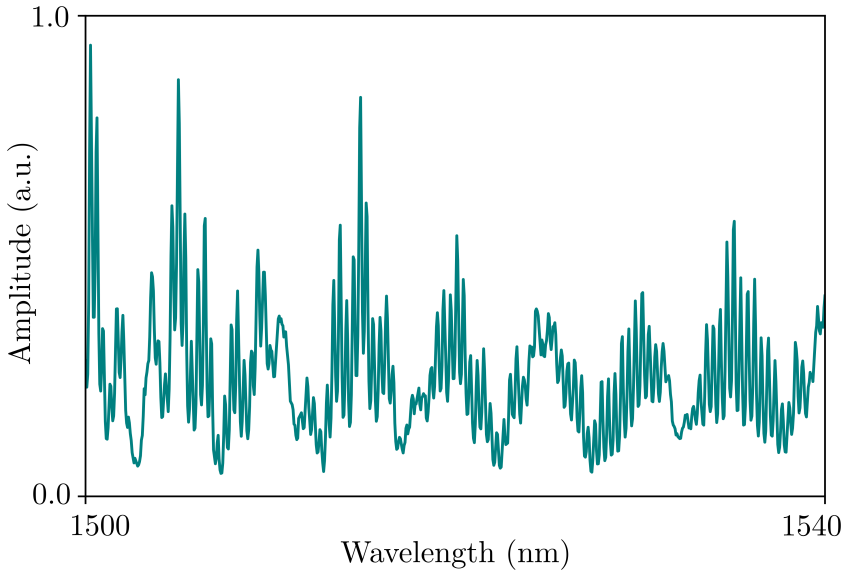

Figure 3.2: Optical spectrum measured at an arbitrary pixel.

After obtaining the experimental results with respect to wavelength, the data were interpolated for angular frequency and the IFT was then calculated to obtain the three-dimensional matrix of interest, $\tilde{I}_{out}(x, y, \tau)$. This matrix contains information about optical intensity for all propagating modes in the time domain. Afterwards, the average of absolute values for all pixels of each image is calculated to obtain the typical IFT curve, as shown in fig. 3.3a. It shows the amplitude oscillations as a function of DGD. The peaks on the IFT curve indicate the beating tones in which the interference pattern generated has a higher optical power. Each peak contains modal information of about the one HOM supported by the fiber that suffers a spectral interference, at a specific group delay, with the fundamental mode or, possibly, with another HOM.

The combination of a 40 nm wavelength window and a 1.66 m fiber length results in a temporal resolution of 0.12 ps/m that is enough to locate five peaks on the IFT curve (fig. 3.3a). These five peaks are highlighted because their normalized amplitude are higher than any other, it means for those DGD values a strong spectral interference occurs between the propagating modes. Thus, when executing the mode recovery step in that peaks, it is possible to recover the mode profiles, intensities and relative phases, of different propagating modes, as show in fig. 3.3b.

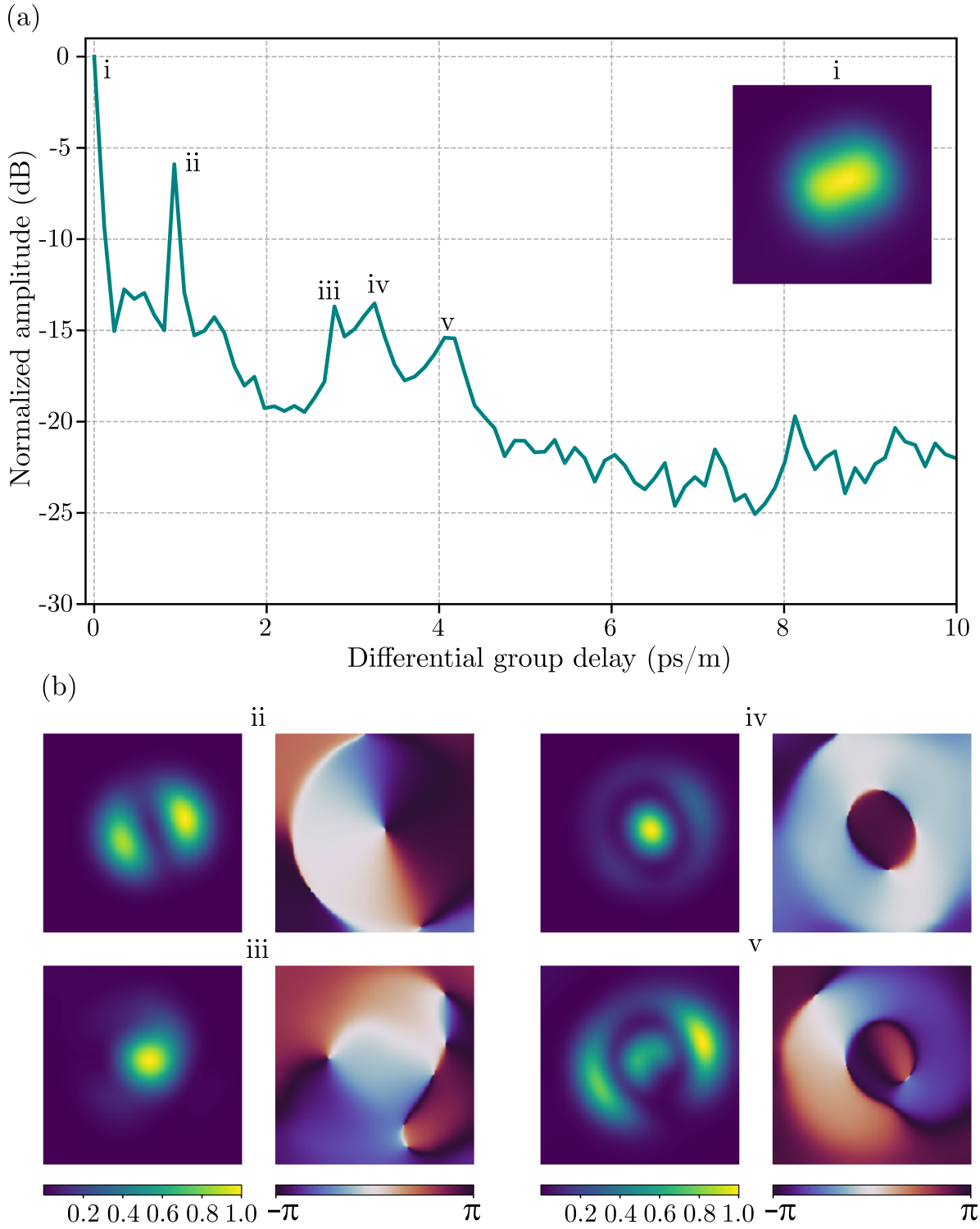

Figure 3.3: S^2 mode recovery in a 1.66 m FMF sample. (a) IFT curve of the optical spectrum measured. The inset in (a) shows the mode intensity profile of the peak (i) that refers to the LP_{01} which is the reference of the experiment. (b) Mode profiles recovered (intensity and relative phase) at the peaks identified in (a) where (b.ii) refers to LP_{11}, (b.iii) is a spurious peak that does not represent a fiber mode, (b.iv) refers to LP_{02} and (b.v) is a peaks resulted from the beating between two HOMs.

The FMF index contrast is 0.55 %, that is considered much less than 1, so the weakly guiding approximation is satisfied and the supported modes by this fiber can be referred to as LP modes. Therefore, the peak (i) with DGD equal to zero refers to the fundamental mode, LP_{01}, that is the reference of the system, so its relative phase is zero. The intensity profile of this mode is shown in the inset of fig. 3.3a. The beam shape recovered is a little flat. This deformation can be attributed to some misalignment of the optical components located between the FMF output and the camera.

The peak (ii) results from the beating tone at a DGD of 0.93 ps/m. By recovering the mode information at this peak, the mode profile shown in fig. 3.3b.ii is obtained. Note the spatial distribution refers to the LP_{11} mode that is supported by the fiber. This HOM overlaps strongly with the fundamental mode so its relative amplitude, of about −6 dB, is considerably high in comparison with other peaks.

The peak (iii) is not a propagation mode. Which was discovered after measurements by using different lengths of the same fiber. It was observed that the group delay of peak (iii) always changes when the fiber length was different. However, if this peak results from a beating tone between the fiber modes, its DGD in ps/m should remain constant independently of the fiber length. So, it can be concluded that this peaks does not refer to a fiber mode.

By investigating the output power of TLS used in the experiment whilst performing a wavelength scan, it was discovered that an intrinsic modulation of the laser power with respect to wavelength leads to the observed peak in the IFT curve. In order to demonstrate how it happens, the S^2 measurement was performed without a fiber, so the coming light from the laser source was directly focused on the camera display using a combination of objective lenses. Figure 3.4 illustrates the experiment executed to demonstrate the peak generated by the laser source.

The result obtained from this measurement is shown in fig. 3.5. Here, it is only presented the IFT curve generated by the S^2 post-processing, where one peak is highlighted. Although there is no optical fiber in this experimental setup, the curve presents a peak at time delay axis equals to 4.62 ps with relative amplitude of about −10 dB. The reason is that this peak is generated due to the intrinsic modulation of the laser power with $\Delta\lambda = 2\lambda^2/c\tau = 3.33$ nm.

In the results obtained by the characterization of the FMF via S^2 method, the peak generated by the laser power modulation is the peak (iii). On the IFT curve (fig. 3.3a), it has a DGD equals to 2.79 ps/m. The normalized DGD is calculated by τ, that is 4.63 ps, divided by the fiber length, that is 1.66 m. The result of this division is equal to 2.79 ps/m, that is exactly the same value of the DGD of the peak (iii). As it does not refer to a fiber mode, its intensity and phase profiles can be dismissed for the fiber characterization.

The peak identified as (iv) refers to a beating tone generated by a spectral

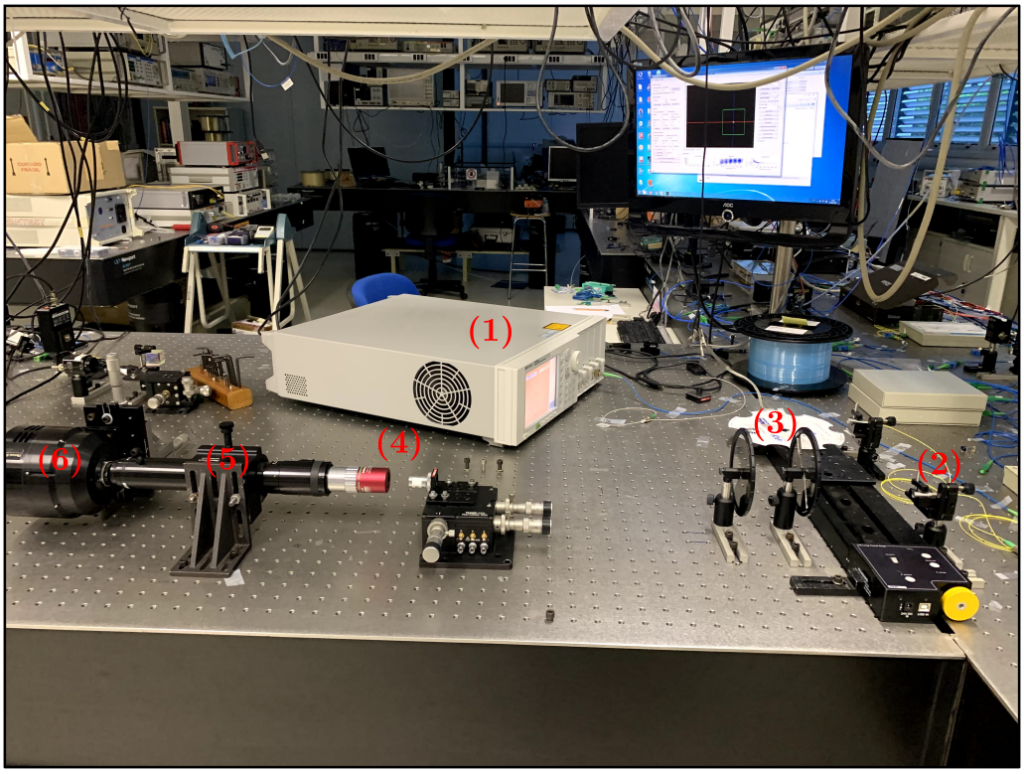

Figure 3.4: Picture of the experimental setup assembled to execute S^2 measurement without a fiber. (1) - Laser source (TLS), (2) - beam expander, (3) - beam attenuators, (4) - 10× and 20× objective lenses, (5) - 12× microscope tube, (6) - InGaAs camera.

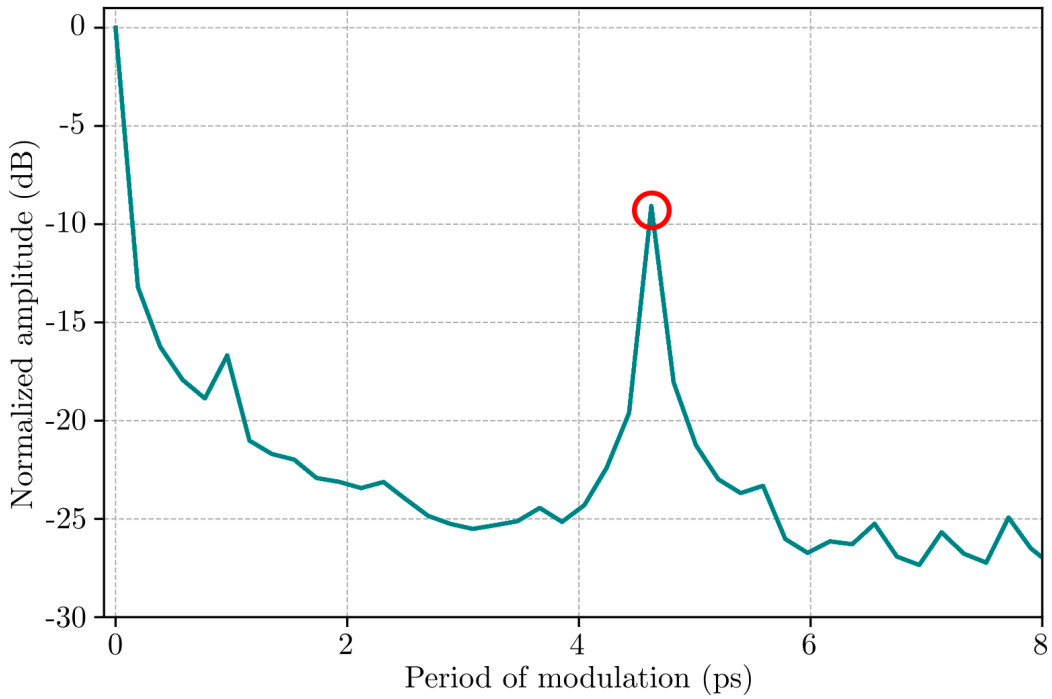

Figure 3.5: IFT curve generated from the S^2 measurement without a fiber. On the curve, it is highlighted the spurious peak.

interference at DGD equals to 3.25 ps/m with a relative amplitude of −14 dB, what means that this mode does not overlap strongly with the fundamental mode as like as the LP_{11} mode. The mode profiles obtained by executing the modal recovery step at this peak are shown in fig. 3.3b.iv. Note that the spatial distribution refers to the LP_{02} mode that was also excited in the fiber.

The peak identified as (v) refers to a beating tone generated by the spectral interference between two HOMs. By observing the spatial distribution in fig. 3.3b.v, it can be concluded that this interference was caused by the beating between the LP_{11} and LP_{02} modes, and leads to a peak at 4.1 ps/m on the IFT curve which corresponds approximately to the DGD of LP_{11} mode plus DGD of LP_{02} mode. Therefore, the appearance of this peak, that is resulted of an interference between these two HOMs, demonstrates experimentally what was discussed in the theoretical description of the S^2 method (section 2.1).

3.2 Simulation step

In this section, the results obtained from the simulation of an approximate geometry of the FMF under analysis will be presented. The simulation is executed using FEM and consists of solving Maxwell's equations by performing the mode analysis under the boundary conditions defined at the fiber cross section. The approximate geometry was defined by means of reverse engineering based on some parameters provided by the fiber manufacturer.

The parameters provided were: core radius, effective index, group index and chromatic dispersion of the LP_{01}, LP_{11} and LP_{02} modes at 1550 nm. Hence, at this point, the objective is to promote a better approximation of the function that governs the fiber refractive index distribution by comparing the given parameters with the results of the simulation. The effective indices and the propagation constants are directly obtained from the mode analysis simulation. Since the propagation constant ($\beta(\omega)$) is known, the group index (N_g) and the chromatic dispersion (σ) of each fiber mode can be calculated as [73]:

$$v_g = \left(\frac{d\beta}{d\omega}\right)^{-1} \tag{3.1}$$

$$N_g = \frac{c}{v_g} \tag{3.2}$$

$$\sigma = -\frac{ck}{\lambda}\frac{d^2\beta}{d\omega^2} \tag{3.3}$$

In which v_g is the group velocity, c is the speed of light in vacuum and k is the wavenumber. A three-point numerical differentiation algorithm was used to calculate the derivative and its details are presented in appendix A. Therefore, the refractive index distribution is a function that depends on two arguments, the wavelength and the fiber radius. The

variation of the silica refractive index with respect to the wavelength was modeled using the Sellmeier coefficients [74].

The radial dependence exists because the core refractive index distribution of this type of fiber has a parabolic profile, like a graded-index fiber. In order to fit the geometry better, a ring was inserted between the core and the cladding with a refractive index lower than the refractive indices of the core and cladding. This lower refractive index ring, also called trench, plays an important role on the chromatic dispersion that is directly related to the group delay of the modes. The trench region was modeled by a normal distribution. The equations (3.4) and (3.5) describe the refractive index distribution modeled for different regions of the fiber cross section.

$$n(r) = n_{core} + (n_{clad} - n_{core}) \left(\frac{r}{r_{core}} \right)^{a}, 0 \leq r \leq r_{core} \tag{3.4}$$

$$n(r) = n_{clad} + (n_{trench} - n_{clad}) e^{-\frac{1}{2}\left(\frac{r-u}{u}\right)^2}, r_{core} < r \leq r_{clad} \tag{3.5}$$

The terms a and u were fitted after several simulation rounds until the results matched with the parameters provided by the fiber manufacturer. Figure 3.6 shows the approximate geometry of the fiber cross section and the refractive index profile modeled.

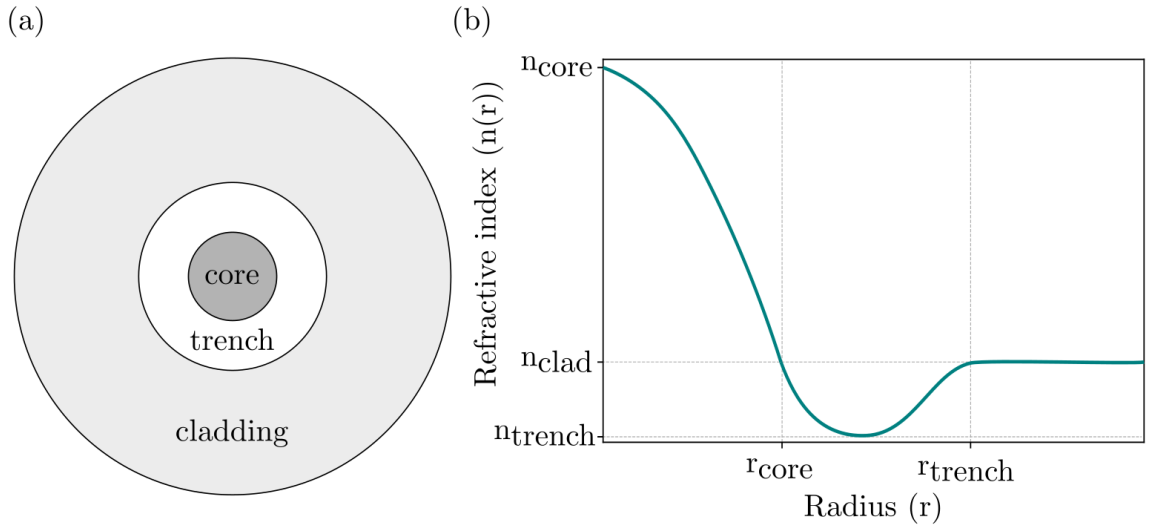

Figure 3.6: Simulation model of an approximate geometry of the FUT. Fiber cross section in (a) and its refractive index distribution in (b).

The fiber core is made of silicon dioxide (SiO_2), also known as silica, doped with a material that increases its refractive index, for example the germanium [74], aiming to allow the optical guiding. As well as the core radius and the index profile, the dopant concentration differentiates the construction features of a specif fiber, determining, for example, its refractive index contrast between the core and the cladding. In the cladding region there is no doping, thus it is built of pure silica that has a lower refractive index than the core. The region between the core and cladding has the lowest refractive index.

This trench region is obtained by doping the silica with a material that decreases its refractive index, for example fluorine [75].

The mode analysis simulation of this fiber geometry was executed to obtain the effective indices and the propagation constants of all supported modes for each wavelength along the simulation frequency range. The fiber supports four LP modes at both SoP, a total of eight propagating modes, that are the fundamental mode, LP_{01}, and two HOMs, the LP_{11} and LP_{02} modes, presented in fig. 3.7. Note the simulation has returned both polarization modes of the LP_{11}, they are LP_{11a} and LP_{11b}, and are degenerate.

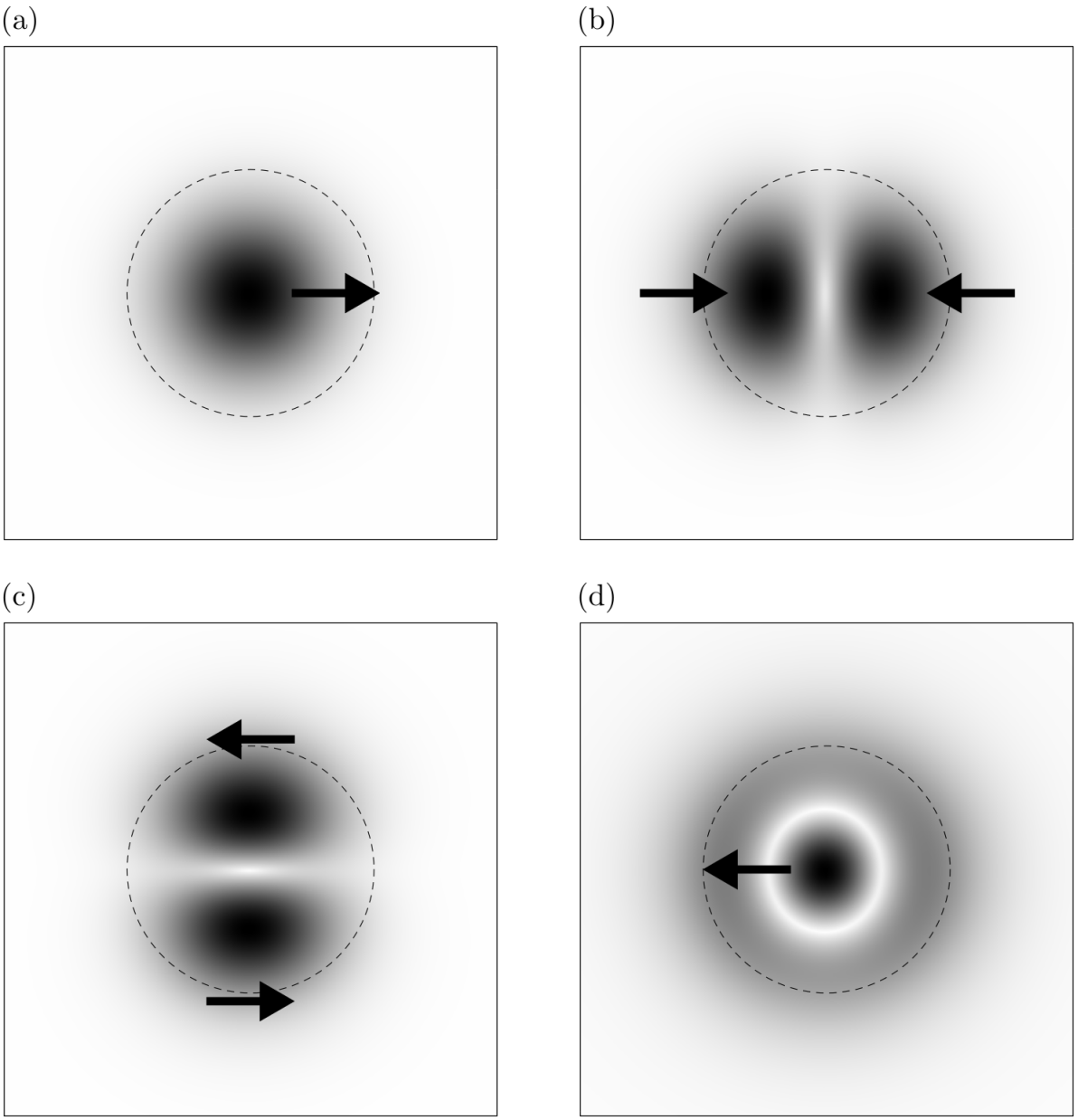

Figure 3.7: Electric field norm at 1550 nm for horizontal polarization and its direction indicated by the arrows. (a) LP_{01} mode. (b) LP_{11a} mode. (c) LP_{11b} mode. (d) LP_{02} mode.

The next step is to evaluate the group indices and the chromatic dispersions of

the modes at 1550 nm by applying the equations (3.1), (3.2) and (3.3). Afterwards we will compare the parameters calculated by the simulation with those parameters provided by the manufacturer. The parameters of interest, effective index, group index and chromatic dispersion, calculated from the simulation results were compared with those provided by the fiber manufacturer by means of relative error evaluation between them, assuming the fiber parameters provided by the manufacturer as the real values.

The relative errors between the real and the calculated values of effective and group indices and chromatic dispersions are lower than 1.5 % for all propagation modes. Since the relative errors between the real and the calculated values are minimal, the fiber geometry modeled in this simulation is considered a good approximation of the real FMF under analysis.

The objective of this simulation is to calculate the theoretical DGDs for all propagating modes to compare this values with the experimental DGDs obtained from the characterization via S^2 method. The DGD between modes m and n with group velocities $v_{g,m}$ and $v_{g,n}$, respectively, travelling in a fiber section with length L is calculated by:

$$\mathrm{DGD} = \frac{L}{v_{g,m}} - \frac{L}{v_{g,n}} \tag{3.6}$$

Since the fundamental mode is the reference, the calculation of the DGD of each HOM is executed with respect to the transit time of fundamental mode. It means that, in eq. (3.6), the m index refers to the LP_{01} and the n index refers to the each HOM. The theoretical and experimental values of DGD are shown in table 3.1.

Table 3.1: Comparison of the differential group delay values

Mode	Calculated DGD [ps/m]	Experimental DGD [ps/m]
LP_{11}	0.83	0.93
LP_{02}	3.59	3.25

For the first HOM, the LP_{11} mode, the theoretical DGD is 0.83 ps/m and the experimental DGD is 0.93 ps/m, therefore the relative error between these values is about 12 %. For the other HOM supported by this FMF, the LP_{02} mode, the theoretical DGD is 3.59 ps/m and the experimental DGD is 3.25 ps/m, therefore the relative error between these values is about 9.5 %. In the literature, it is demonstrated the application of the S^2 method to recover HOMs of a photonic-bandgap fiber, obtaining relative errors between the theoretical and experimental DGD values of 8 % and 12.5 % for the LP_{11} mode [69].

Therefore, it can be conclude the results obtained from the FMF characterization are validated and the simulation reflects an adequate fitting of the real FUT. The differences between the results are due to the fact that all simulation, even when well fitted, is an approximation. Moreover, some fabrication aspects can impact the optical characteristics

of the fiber such as eccentricity and geometrical variations along the fiber length. These aspects will have a direct impact in the final values, particularly considering quantities that depend on the first or second derivatives of the fiber dispersion characteristics.

Chapter 4

Coupler characterization via S^2 method

This chapter presents the results obtained from the modal characterization of a photonic coupler developed by GEMAC team. The device was designed to perform the coupling interface between SMFs and the FMF under study in this work. After performing the modal characterization of the FMF as exposed in Chapter 3, we apply the S^2 method to characterize the PIC in order to analyze and show its operation.

Initially, the main features, design and principle of operation of the device will be describe based on the paper published by Ruiz *et al.* [76], that explains the development of the coupler. After that, we will explain the experimental setup employed to recover the HOMs excited by the device into the FMF. Finally, the experimental results obtained from the characterization using the S^2 method will be present and discussed.

4.1 Tri-modal coupler overview

The device proposed by Ruiz *et al.* [76] was developed to couple the light between the PIC and the FMF under study. It was built in a SOI platform compatible with CMOS technology. The SOI chip is composed of three layers: a device layer of 250 nm thickness, a buried silicon dioxide layer of 3 µm thickness and a silicon dioxide cladding layer of 1 µm thickness. The coupling interface between the chip and the fiber is performed through grating couplers that are periodic structures able to diffract the light that propagates in the same plane of the waveguide to free-space, out-of-plane of the SOI chip [77].

The device was designed to couple three transverse modes of light propagation. The fundamental mode, LP_{01}, and two HOMs, LP_{11a} and LP_{11b}, that are supported modes by the FUT at wavelength of 1550 nm, as shown in section 3.2. It couples the light to the FMF oriented in the orthogonal direction to the chip plane through a bidirectional

nonuniform diffraction grating. Its capacity to diffract light in the vertical direction has the advantage of eliminating any polishing angle on the fiber, making the alignment straightforward [76].

In addition to the grating mentioned before, the tri-modal coupler consists of two identical in-plane modal multiplexers, connected at both sides of the bidirectional grating using two adiabatic tapers. The two adiabatic tapers have a 22 µm × 250 nm cross section and are responsible to excite the TE_0 and TE_1 waveguide modes that are coupled into the LP_{01x}, LP_{11ax} and LP_{11bx} propagation modes of the FMF [76].

The design of the bidirectional nonuniform grating coupler just enables the coupling of the modes at a single SoP due to its structural limitation. Nonetheless, its design could be extended to a two-dimensional grating configuration by superimposing two identical structures [78] to perform the coupling at both SoP, thus becoming able to address six modes of light propagation.

In addition to the grating/port in which the FMF is coupled vertically, the device has other four grating couplers that are used to couple light coming from SMFs. These gratings/ports are connected to the inputs of the two modal multiplexers. The excitation port will excite different waveguide modes that will be coupled into the FMF at the output. The single-mode grating couplers at these inputs ports were optimized to perform the light coupling in a 10° angle.

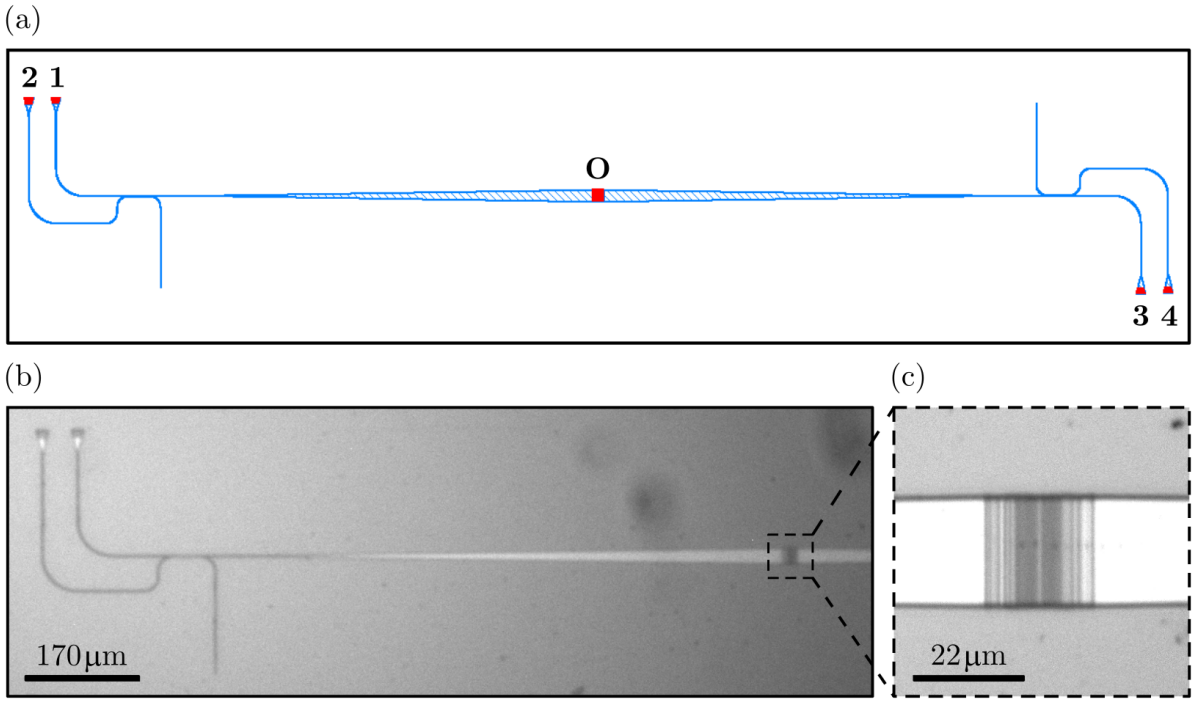

Figure 4.1: Representation of the tri-modal coupler. (a) Device schematic with the identification of the gratings/ports. (b) Microscope image of one side of the fabricated coupler. (c) Microscope detailed image of the bidirectional nonuniform grating.

Figure 4.1 is a graphic representation of the device under analysis including

microscope images. Figure 4.1a is a computer aided design (CAD) schematic of the device, where is possible to observe the two modal multiplexers, that are connected at the ports identified from 1 to 4, where SMFs are coupled. Moreover, it shows the two adiabatic tapers that connect the modal multiplexers to the bidirectional nonuniform grating, identified as port O.

Figure 4.1b and 4.1c are microscope images of the fabricated coupler, detailing the grating where the FMF is coupled. The two adiabatic tapers, that connect the both sides of the FMF grating to the two modal multiplexers, are 703 µm long by 930 nm wide. The inputs/outputs waveguide cross sections of both modal multiplexers are 450 nm × 250 nm with a gap separation of 200 nm.

The device was designed to allow the addressing of the FMF propagating modes that are coupled into the waveguide modes (on the SOI chip) and directed towards the single-mode gratings. The modal multiplexers execute the mode selection and direct them to their corresponding port. It means the LP_{01x} and LP_{11bx} modes are directed toward the ports 1 and 3, and the LP_{11ax} mode is directed towards the ports 2 and 4, according to fig. 4.1a. Since the device is reciprocal, the reverse path is also valid.

Ruiz *et al.* [76] have performed an experimental setup at LCO/Photonicamp to characterize the coupling efficiencies of the fabricated coupler. In the experiment, the device was fed by the FMF positioned out-of-plane and vertically to the bidirectional grating. A spatial light modulator (SLM) was also applied in order to excite the FMF propagating modes independently. Each mode, LP_{01x}, LP_{11ax} and LP_{11bx}, was coupled into the device at a time and its power was measured by a power meter connected in the SMFs positioned on the single-mode grating output ports.

To measure the coupling efficiency of the LP_{01x} mode, the corresponding phase mask was imprinted on the SLM display and the powers measured at the ports 1 and 3 were added, normalized according to the input power, and discounted the coupling loss of the single-mode grating. The coupling efficiency of the LP_{11bx} was measured following the same process, just changing the phase mask on the SLM. For the measurement of the LP_{11ax} mode, the corresponding phase mask was inserted on the SLM and the output powers were measured at the ports 2 and 4 [76].

Table 4.1: Coupling efficiencies of the modes.

Mode	Coupling efficiency (dB)
LP_{01x}	-3.0
LP_{11ax}	-3.6
LP_{11bx}	-3.4

Table 4.1 shows the maximum coupling efficiencies measured by the experiment [76]. As mentioned before, the device was designed for the maximum coupling

efficiencies at 1550 nm. However, due to manufacturing errors, it was observed a wavelength shift to values near 1520 nm for which the device is more efficient. Another point to be highlighted is the FMF grating coupler was optimized to couple all the three LP modes with similar efficiencies. From the table 4.1, we can infer a mode-dependent loss (MDL) of 0.6 dB.

Due to its reciprocity, the coupling efficiency values are the same for both direction of operation, with the light coming from the FMF to the chip, as used at the mentioned experiment, and for the light coming from the chip to the FMF [76]. The last was the direction applied in the S^2 experiment performed in this work in order to recover the modal content at the output of the FMF when we change the excitation ports of the device.

4.2 Experiment including the coupler

In this section, we present the experiment implemented to perform the modal content characterization via S^2 method at the FMF output when is excited by the tri-modal coupler developed by our research group. The experimental setup was assembled in the Laboratory of Applied and Computational Electromagnetics (LEMAC) located at Photonicamp.

Figure 4.2 presents the scheme of the experimental setup implemented in order to include the tri-modal coupler. The setup is similar to that present in section 2.2, when the FUT was excited by a SMF, and follows the same approach already applied to characterize the FMF individually. The change was to use the SOI chip to excite the LP modes of the fiber.

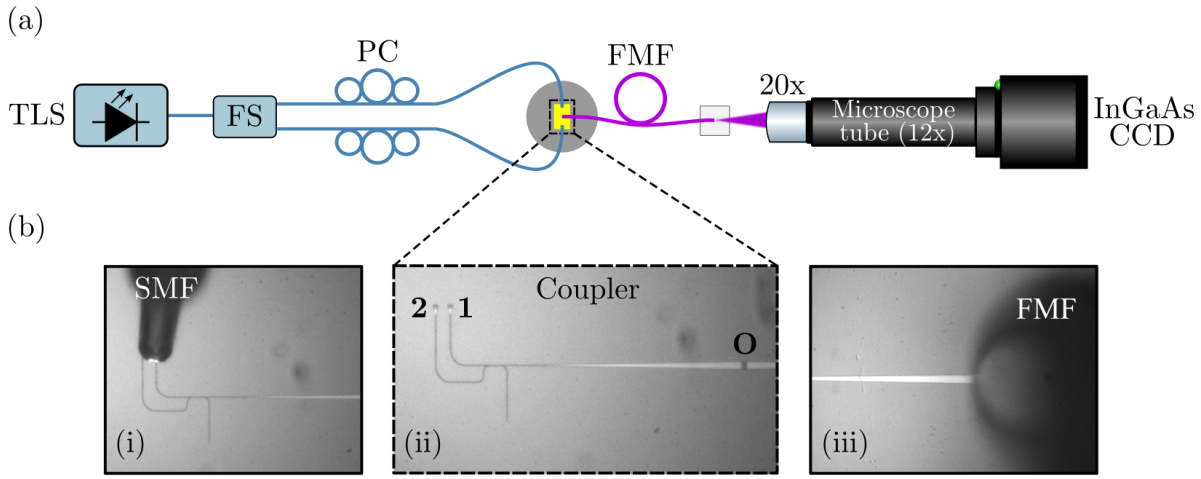

Figure 4.2: Experimental implementation for modal characterization including the coupler. (a) Scheme of the experimental setup. (b) Microscope images of the coupler with the identification of the ports, and the positioning of the optical fibers over the grating couplers in detail.

The TLS, fig. 4.2a, is a Continuously Tunable Laser from Toptica Photonics and is used to perform the wavelength scan inside a pre-defined spectral window. The light coming out of the laser is coupled to a fiber splitter (FS) to divide the input power equally to two output SMFs. A polarization controller (PC) is used to adjust the appropriate orientation of the electric field at the inputs of the device.

The SMFs are aligned over the single-mode gratings, the maximum coupling efficiency occurs when the SMFs are positioned at 10° angle with respect to the normal to chip plane. The light is then coupled to the chip that is positioned on a rotation stage. The output grating of the device diffracts the light that is then coupled to the FMF, vertically aligned. The FMF length is 1.53 m.

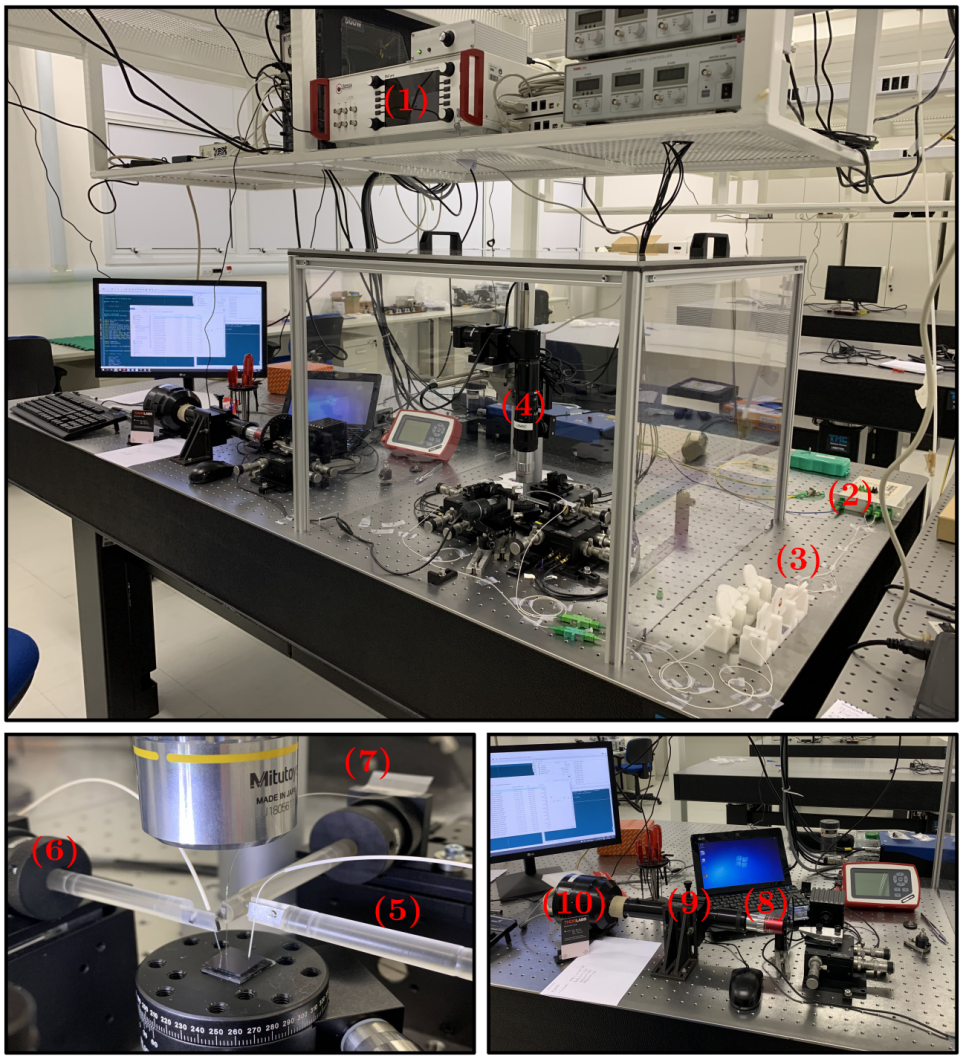

Figure 4.3: Picture of the experimental setup assembled at LEMAC/Photonicamp to execute the S^2 characterization of the FMF when is excited by the tri-modal coupler. (1) - TLS, (2) - fiber splitter, (3) - polarization controllers, (4) - Microscope, (5) and (6) - SMFs holders, (7) - FMF holder, (8) - 20× objective lens, (9) - 12× microscope tube and (10) - InGaAs camera.

The FMF output beam is then magnified by a 20× objective lens connected

to a 12× microscope tube. Finally, the beam profiles are captured by the InGaAs CCD camera from Photonic Science. The data are recorded in a three-dimensional matrix containing the pixels matrices of the images for each wavelength set by the TLS.

Figure 4.2b shows microscope images taken during the experiment, detailing the alignment of the SMFs over the ports 1 to 4 (same identification shown at fig. 4.1a), and the FMF over port O. Initially, the experiment was performed only exciting the chip by one input port at a time. After, two sets of measurements were carried out and, in both of them, two input ports of the device were excited simultaneously. In one measurement both ports 1 and 3 were excited, and in the second, both ports 2 and 4. The ports 3 and 4 are located at the other side of the coupler.

A power meter is also employed to measure the optical power at the FMF output to help us during the alignment of the system. When the power measured is maximum, the FMF output beam is then directed to the InGaAs sensor and the wavelength scan starts. Figure 4.3 illustrates the experimental setup, identifying the equipment used. The alignment stage on the SOI chip is assembled inside an acrylic box due to the system sensitivity to external disturbances.

A microscope equipped with a 5× objective lens and a visible light camera, and a digital USB microscope are used during the positioning of the optical fibers over the grating couplers. Specific acrylic holders were fabricated due to the need to approximate three fibers over the SOI chip in a limited space. The fibers are also held by 3-axis alignment stages with piezoelectric controllers.

4.3 Experimental results

This section presents the experimental results achieved by the modal content characterization of the FMF output when is excited by the tri-modal coupler. A TLS is also used to perform a wavelength scan inside a pre-defined spectral window. Hence, the first step is to find the proper wavelength spectral window to execute the S^2 experiment.

The spectral window is defined according to the wavelength range of the best operation of the device. In order to find the best wavelength range, we employ the experimental setup shown in fig. 4.2 with a power meter at the FMF output instead of the CCD camera. So that, the optical power could be measured while the TLS was executing the wavelength scan. The best operation was achieved inside a wavelength window from 1520 nm to 1540 nm.

The first S^2 measurement was performed by exciting the device by only one input at a time. To do this, the outputs of the fiber splitter were uncoupled of the SMFs inputs alternately, thus controlling the excitation port of the coupler. The results obtained by exciting the ports located at one side of the device, i.e. the inputs of one modal multiplexer, are similar to that obtained by exciting the inputs of the other modal

multiplexer, located on the other side of the chip. Therefore, we present the results obtained when the device is excited by the ports 1 and 2 (see the identification of the ports in fig. 4.2b.ii).

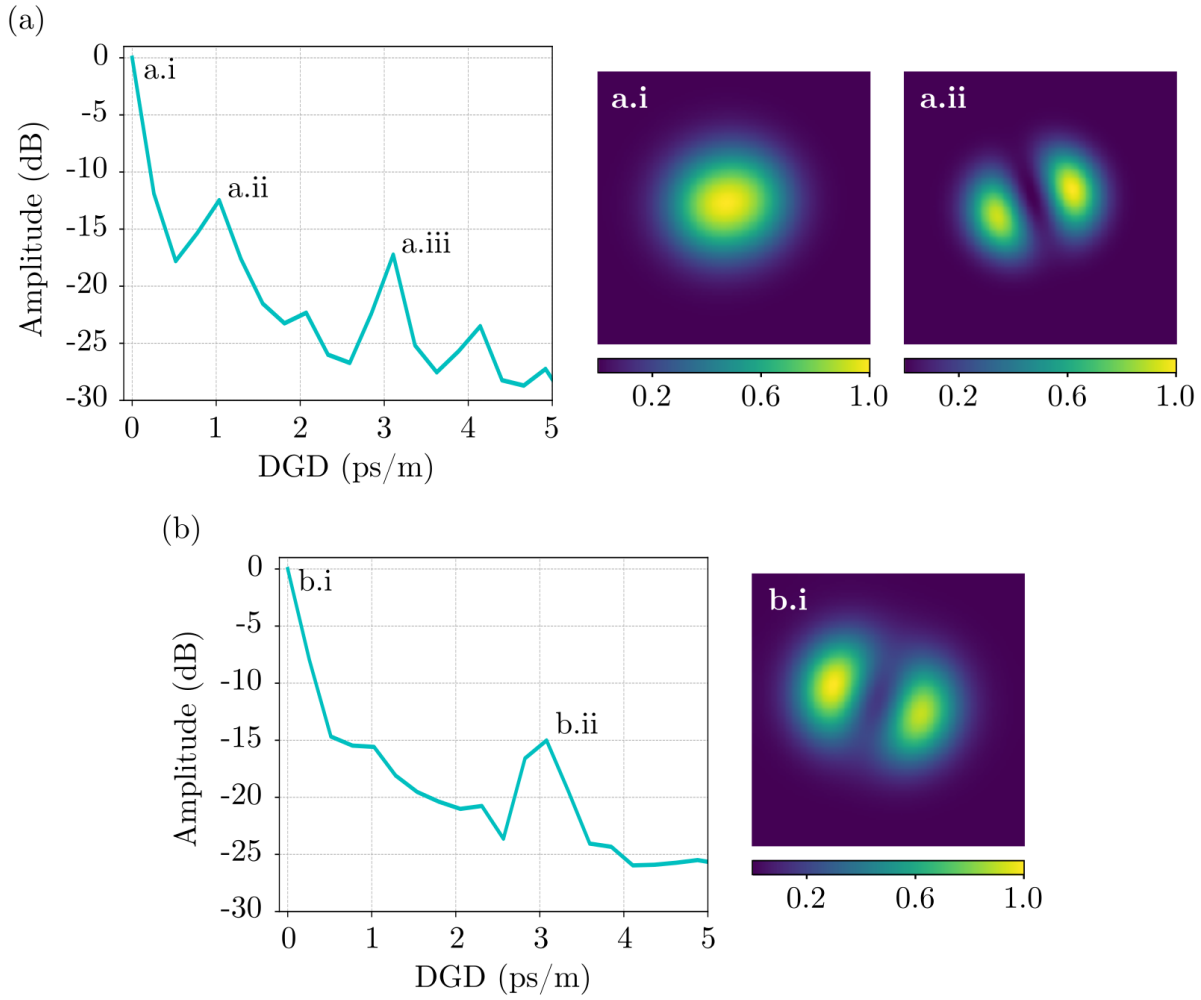

Figure 4.4: S^2 mode recovery at the FMF output when the coupler is fed by a single input port. (a) IFT curve and mode profiles of the peaks for excitation port 1. (b) IFT curve and mode profile of the peak for excitation port 2.

Figure 4.4 shows the results obtained from the first implementation of the S^2 method including the coupler, by using a single input at a time. As mentioned before, the wavelength window extends from 1520 nm to 1540 nm. Therefore the combination of the 20 nm wavelength window and the 1.53 m fiber length results in a temporal resolution of 0.26 ps/m. That is enough to place three peaks on the IFT curve when the device is excited by input port 1, fig. 4.4a, and two peaks on the IFT curve when the device is excited by input port 2, fig. 4.4b.

The temporal resolution is not high, which is why the peaks represented on the IFT curve are wide. This drawback was assumed because we are interested in locating peaks that represent some propagating mode instead of getting an extremely accurate DGD value. Furthermore, if we set a larger wavelength window on the TLS in order to improve

the temporal resolution, the measurement duration becomes longer, thus increasing the experiment error due to external disturbances. Moreover, the excitation of HOMs using the coupler becomes even more sensitive to instabilities, and then the measurement needs to be faster. For the measurement using only one input port at a time, the continuous sweep speed of the laser was 0.5 nm/s.

By observing the mode profiles in fig. 4.4a, the peak (a.i) with DGD equals to zero refers to the fundamental mode, LP_{01}, that is the reference of the system and the fastest mode to propagate along the fiber sample. The peak (a.ii) refers to the LP_{11b} mode that spectrally interfered with the fundamental mode with a DGD of about 1.0 ps/m. The peak (a.iii) does not refer to a HOM, it is actually a spurious peak. More details about it will be explained in the following.

When performing the measurement by exciting the device on port 2, the results shown in fig. 4.4b were obtained. The peak (b.i) is the only mode excited into the FMF. Since the adjustment of the polarization controllers of both SMFs inputs was kept during the two measurements performed, this peak does not refer to the same HOM recovered in another SoP. Therefore, it refers to the LP_{11a} mode as we expected. The peak (b.ii) is also a spurious peak and its existence is explained by the same reason of the peak (a.iii).

Similarly to the experiment performed to characterize the modal content when the FMF was directly excited by a SMF, the peaks (a.iii), generated when exciting the device on port 1, and (b.ii), generated when exciting on port 2, also refer to an intrinsic modulation of the TLS power with respect to wavelength. Both peaks (a.iii) and (b.ii) have a DGD of about 3.1 ps/m. Since the fiber length is 1.53 m, the period of modulation corresponds to 4.7 ps.

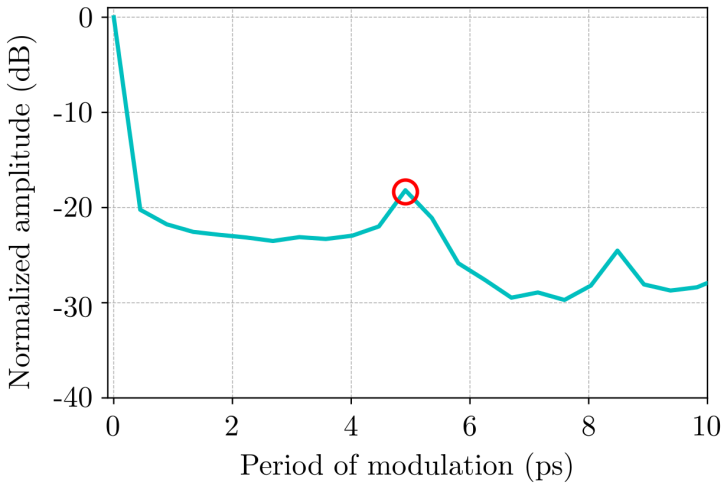

Figure 4.5: IFT curve generated from the S^2 measurement without coupler and fiber. On the curve, the spurious peak is highlighted .

In order to evaluate the intrinsic modulation of the laser from Toptica Photonics, we execute the S^2 experiment without the coupler and fiber, as well as it was done for

the laser from Agilent Technologies, used in section 3.1. The result obtained confirms the existence of an intrinsic modulation of this laser that leads to a peak on the IFT curve with time delay equals to 4.9 ps and it is highlighted in fig. 4.5. The difference of 0.2 ps is irrelevant, and can be attributed to some small difference of the order of centimeters in the fiber length.

After executing this first experimental implementation, it was already possible to confirm the proper operation of the device according to the its design, explained in section 4.1. The LP_{01} and LP_{11b} modes could be recovered at the FMF output when the coupler was fed individually by the SMFs gratings identified as ports 1 and 3. The LP_{11a} could be recovered when the coupler was fed individually by the SMFs gratings identified as ports 2 and 4. Therefore, three light propagation modes could be recovered at a single SoP as we expected.

So far, the operation of the device was analyzed using only one input port at a time by alternating the active output of the fiber splitter. Now, the objective is to implement the full experiment by exciting two input ports simultaneously. The excitation ports are defined according to the design of the coupler, in such way, that one measurement is taken by exciting both ports 1 and 3, and other is taken by exciting both ports 2 and 4, following the identification of the ports shown in fig. 4.1.

Some points observed during the alignment of the fibers to execute the new measurement should be highlighted. The difference of phase between the two SMFs inputs leads to experimental instabilities, especially when we excite the device by the ports 1 and 3. When these two inputs are in-phase, a constructive interference is generated, and the LP_{01} mode is excited into the FMF. When they are out-of-phase, the LP_{11b} mode is excited.

As no phase control method of the inputs was applied, the FMF output beam monitored by the CCD camera was unstable. The beam fluctuation has impacted the measurement directly, because the S^2 method needs the reference of the system to be stable. Therefore, the solution to this problem was to accelerate the continuous sweep speed of the laser. Previously, the speed used was 0.5 nm/s, now we set 5 nm/s. Since the wavelength window is 20 nm, the measurement took only four seconds.

Figure 4.6 presents the results obtained from the S^2 measurements while the coupler was excited by combining two input ports. It was possible to identify two peaks on the IFT curve when the device was excited by both ports 1 and 3, as illustrated in fig. 4.6a. By recovering the modal content for these DGD values it could be observed the mode profiles of the LP_{01}, represented by peak (a.i), and LP_{11b} modes, represented by peak (a.ii), what agrees to the expected device behavior. The DGD value of the HOM recovered is of about 1.0 ps/m too.

In fig. 4.6b, when the excitation ports were switched for ports 2 and 4, only one peak appeared on the IFT curve. As the polarization controllers adjustment was kept,

this peak refers to another HOM. Therefore, peak (b.i) represents the LP_{11a} mode that was the only one excited by the coupler into the FMF, what confirms the proper operation of the device.

A point to be highlighted is for the TLS continuous sweep speed of 5 nm/s, the spurious peak was not observed. This happened because a faster scan speed affects the resolution with respect to wavelength, because it increases the sweep step. Therefore, the intrinsic modulation of the laser cannot be perceived with fewer wavelength values being captured during the experiment.

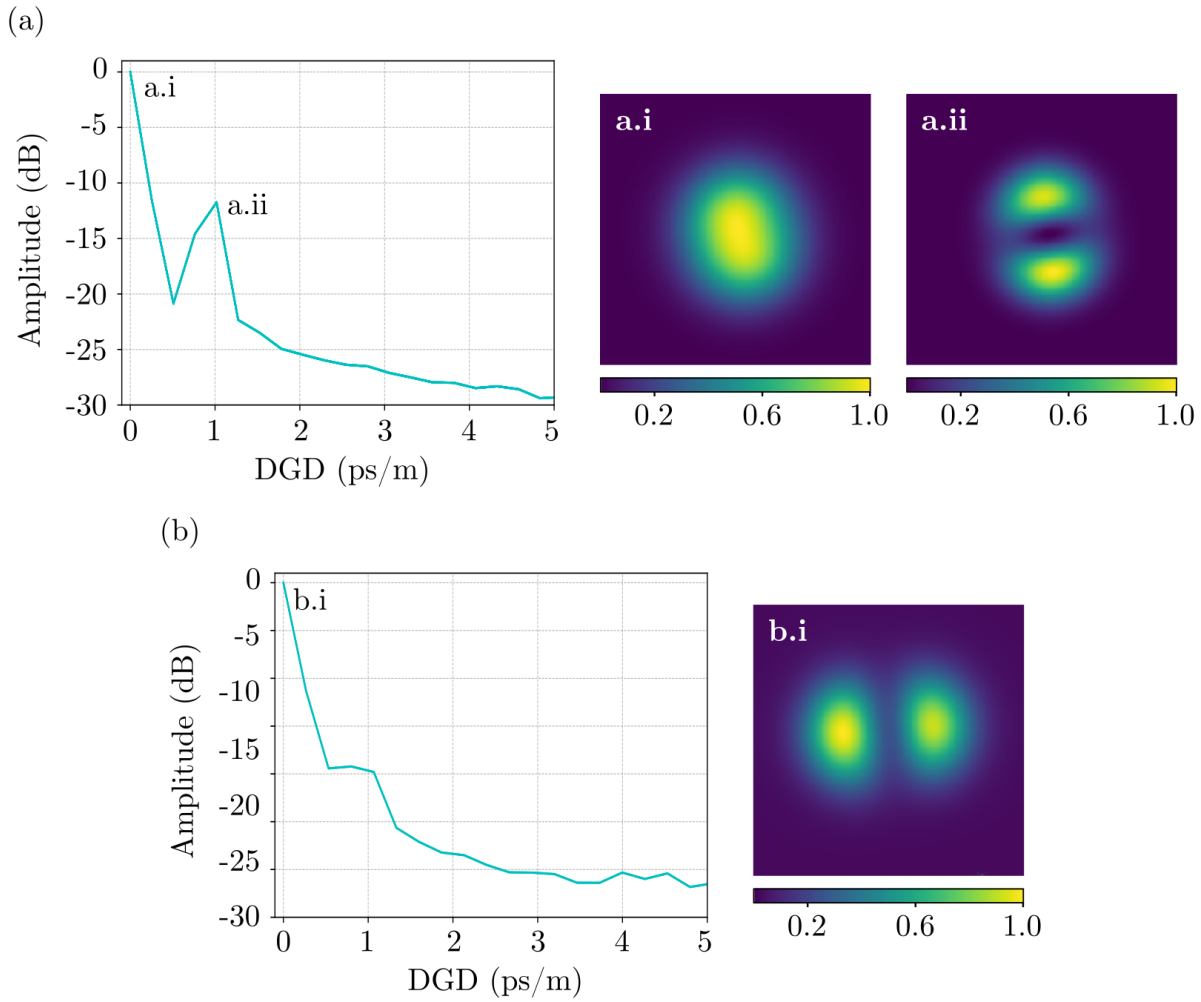

Figure 4.6: S^2 mode recovery at the FMF output when the coupler is fed by two input ports simultaneously. (a) IFT curve and mode profiles of the peaks for combined excitation of ports 1 and 3. (b) IFT curve and mode profile of the peak for combined excitation of ports 2 and 4.

Although the resolution with respect to wavelength has been affected, it was possible to solve the phase instability problems to enable the recovery of the light propagation modes at the FMF output when the coupler were excited by two ports simultaneously. Therefore, the operation of the device could be validated from the S^2 results by observing the modal content of the FMF while the coupler excited it. Note the fiber also supports

the LP_{02} mode as we demonstrate experimentally in Chapter 3. However, this mode was not recovered, because the coupler was not designed to excite this HOM into the FMF.

Another important consideration is about the DGD values measured in all experiments including the coupler. The DGD axis on the IFT curve is not so accurate. In these experiments, the DGD does not depend only on the FUT, as in the case of the S^2 method applied to characterize optical fibers, because the propagation constants of the modes into the PIC waveguides affect these values.

In addition to the contribution in the group delay of the fiber, the contributions of propagation delays inherent to the phase shift of the electric field into the coupler waveguides must be considered. Therefore if a precise DGD value is required, these contributions also should be considered together with the fiber length. In this work, the most relevant point is to demonstrate the application of the S^2 method to recover the field profiles of the optical modes to perform a complete modal content characterization including PICs.

Chapter 5

Conclusion

This work has address the subject of the Optical Communications, especially the technologies embedded in SDM systems. The focus was given around optical devices that has been research subject of the scientific community to support the implementation of MDM systems, in which the transverse modes of light propagation are employed as data transmission channels.

A type of these devices was studied in this work, the FMFs that are optical fibers developed with a special geometry in order to support the propagation of few optical modes. And multimode photonic couplers, especially those built in SOI platform, in our case a device capable of coupling three modes was developed by our research group to be the interface coupling between a chip and the FMF under analysis.

In order to characterize the modal content of these devices, different methods proposed in the literature were listed. One of those methods based on the Fourier Transform was choose due to its robustness. The S^2 method demands a relatively simple experimental setup in comparison with others employed to perform modal content characterization. Nonetheless, the algorithm used to implement the experimental data post-processing is complex and has demanded a long time to be understood.

A detailed explanation about the theory, principle of operation and experimental implementation of the S^2 method was accomplished. The basic mathematical equations of the method were exposed according to the literature, showing how the group delay between propagation modes lead to a spectral interferences between the HOMs and the fundamental mode. These interferences can be seen as peaks in a curve generated on the time domain after the application of Inverse Fourier Transform. In addition, an improvement focused on detailing mathematically the spectral interferences that occur between two HOMs was demonstrated.

After the theoretical discussion, we present the known experimental setup employed by other works in the literature to characterize the modal content of optical fibers. All steps were detailed individually in order to expose the measurement process and the post-processing performed by the S^2 algorithm. Then, the experimental limitations of

the method were described. They are related to the computational memory consumption, signal sampling frequency and temporal resolution.

A correlation and dependance between the experimental limitations was established in order to achieve proper experimental conditions for the characterization of the FMF under test. Considering this, robust experimental results were obtained and it was demonstrated a complete recovery of all LP modes supported by the FUT, that were the LP_{01}, LP_{11} and LP_{02} modes. Furthermore, it was shown a beating tone generated by the spectral interference between two HOMs.

In addition, a spurious peak that appeared on the IFT curve was investigated. This peak did not have a fixed group delay, in fact its position with respect to the DGD axis changed with the fiber length. Therefore, we discovered that an intrinsic modulation of power of the TLS with respected to the wavelength was generated whilst it performed the sweeps during the measurements. This modulation caused a beating tone that led to a peak on the IFT curve.

To better interpret the achieved results from the FMF characterization, an approximate geometry of the FUT was modeled using the FEM. After find an adequate fitting for the refractive index distribution, the effective and group indices, chromatic dispersions and DGD values of the modes were calculated by applying a three-point numerical differentiation algorithm. Some fabrication aspects and calculation approximations influenced the calculated DGD values that diverged a little from the experimental values. The maximum relative error between the experimental and calculated DGD values for LP_{11} mode is about 12 %. This value is in agreement with similar published in the literature, therefore the experimental results are validated.

Finally, for the best of our knowledge, we proposed the implementation of the S^2 method to characterize the modal content of the FMF when it is excited by a tri-modal coupler that was developed by our research group. The PIC was built in a SOI platform and enabled the coupling of LP modes from chip to fiber by employing integrated devices, e.g., a bidirectional nonuniform grating, modal multiplexers and other devices.

The S^2 method was able to recover the modal profiles of the propagation modes expected for each one of the input ports of the coupler that was being excited, as well as for their combination, thus validating the proper operation of the device. However, in this experimental scenario, the DGD values are not so accurate due to the contribution of propagation delays added by the coupler waveguides. A dedicated study about the impact of an external excitation device in the DGD values measured by the S^2 method at the output of the fiber can be approached in the future.

Furthermore, a phase control method can be employed in the experimental setup to solve the instability problems arising from the phase difference of the inputs when the coupler is excited by two ports simultaneously. With a more stable experimental condition, it will be possible to improve both the wavelength resolution, by using a slowest

continuous wavelength sweep speed, and the temporal resolution, by defining a larger wavelength window on the laser.

References

[1] G. P. Agrawal, *Fiber-Optic Communication Systems*, vol. 222. John Wiley & Sons, 2010.

[2] R. J. Sanferrare, "Terrestrial lightwave systems," *AT&T technical journal*, vol. 66, no. 1, pp. 95–107, 1987. DOI: https://doi.org/10.1002/j.1538-7305.1987.tb00478.x.

[3] D. Gloge, A. Albanese, C. Burrus, E. Chinnock, J. Copeland, A. Dentai, T. Lee, T. Li, and K. Ogawa, "High-speed digital lightwave communication using leds and pin photodiodes at 1.3 μm," *Bell System Technical Journal*, vol. 59, no. 8, pp. 1365–1382, 1980. DOI: https://doi.org/10.1002/j.1538-7305.1980.tb03369.x.

[4] M. Horiguchi and H. Osanai, "Spectral losses of low-OH-content optical fibres," *Electronics Letters*, vol. 12, no. 12, pp. 310–312, 1976. DOI: https://doi.org/10.1049/el:19760239.

[5] M. Kawachi, A. Kawana, and T. Miyashita, "Low-loss single-mode fibre at the material-dispersion-free wavelength of 1.27 μm," *Electronics Letters*, vol. 13, no. 15, pp. 442–443, 1977. DOI: https://doi.org/10.1049/el:19770320.

[6] J. Yamada, S. Machida, and T. Kimura, "2 Gbit/s optical transmission experiments at 1.3 μm with 44 km single-mode fibre," *Electronics Letters*, vol. 17, no. 13, pp. 479–480, 1981. DOI: https://doi.org/10.1049/el:19810334.

[7] T. Miya, Y. Terunuma, T. Hosaka, and T. Miyashita, "Ultimate low-loss single-mode fibre at 1.55 μm," *Electronics Letters*, vol. 15, no. 4, pp. 106–108, 1979. DOI: https://doi.org/10.1049/el:19790077.

[8] A. Gnauck, B. Kasper, R. Linke, R. Dawson, T. Koch, T. Bridges, E. Burkhardt, R. Yen, D. Wilt, J. Campbell, *et al.*, "4-Gbit/s transmission over 103 km of optical fiber using a novel electronic multiplexer/demultiplexer," *Journal of lightwave technology*, vol. 3, no. 5, pp. 1032–1035, 1985. DOI: https://doi.org/10.1109/JLT.1985.1074318.

[9] T. Okoshi, "Recent advances in coherent optical fiber communication systems," *Journal of lightwave technology*, vol. 5, no. 1, pp. 44–52, 1987. DOI: https://doi.org/10.1109/JLT.1987.1075396.

[10] R. A. Linke and A. H. Gnauck, "High-capacity coherent lightwave systems," *Journal of Lightwave Technology*, vol. 6, no. 11, pp. 1750–1769, 1988. DOI: https://doi.org/10.1109/50.9992.

[11] M. Nakazawa, Y. Kimura, and K. Suzuki, "Efficient Er3+-doped optical fiber amplifier pumped by a 1.48 μm InGaAsP laser diode," *Applied physics letters*, vol. 54, no. 4, pp. 295–297, 1989. DOI: https://doi.org/10.1063/1.101448.

[12] T. Li, "The impact of optical amplifiers on long-distance lightwave telecommunications," *Proceedings of the IEEE*, vol. 81, no. 11, pp. 1568–1579, 1993. DOI: https://doi.org/10.1109/5.247728.

[13] T. Otani, K. Goto, H. Abe, M. Tanaka, H. Yamamoto, and H. Wakabayashi, "5.3 Gbit/s 11300 km data transmission using actual submarine cables and repeaters," *Electronics Letters*, vol. 31, no. 5, pp. 380–381, 1995. DOI: https://doi.org/10.1049/el:19950271.

[14] "Submarine Cable Map." Provided by TeleGeography. Available in https://www.submarinecablemap.com/. Visited on 08/23/2021.

[15] P. Hansen, L. Eskildsen, S. Grubb, A. Stentz, T. Strasser, J. Judkins, J. DeMarco, R. Pedrazzani, and D. DiGiovanni, "Capacity upgrades of transmission systems by raman amplification," *IEEE Photonics Technology Letters*, vol. 9, no. 2, pp. 262–264, 1997. DOI: https://doi.org/10.1109/68.553113.

[16] K. Fukuchi, T. Kasamatsu, M. Morie, R. Ohhira, T. Ito, K. Sekiya, D. Ogasahara, and T. Ono, "10.92-Tb/s (273× 40-Gb/s) triple-band/ultra-dense WDM optical-repeatered transmission experiment," in *Optical Fiber Communication Conference*, p. PD24, Optical Society of America, 2001. DOI: https://doi.org/10.1364/OFC.2001.PD24.

[17] G. Vareille, F. Pitel, and J. Marcerou, "3tbit/s (300× 11.6 gbit/s) transmission over 7380 km using c+ l band with 25ghz channel spacing and nrz format," in *Optical Fiber Communication Conference*, p. PD22, Optical Society of America, 2001. DOI: https://doi.org/10.1364/OFC.2001.PD22.

[18] P. J. Winzer and R.-J. Essiambre, "Advanced modulation formats for high-capacity optical transport networks," *Journal of Lightwave Technology*, vol. 24, no. 12, pp. 4711–4728, 2006. DOI: https://doi.org/10.1109/JLT.2006.885260.

[19] Z. Pan, K. Liang, Q. Ye, H. Cai, R. Qu, and Z. Fang, "Phase-sensitive otdr system based on digital coherent detection," in *Asia Communications and Photonics Conference and Exhibition*, p. 83110S, Optical Society of America, 2011. DOI: https://doi.org/10.1364/ACP.2011.83110S.

[20] X. Zhou, J. Yu, M.-F. Huang, Y. Shao, T. Wang, L. Nelson, P. Magill, M. Birk, P. I. Borel, D. W. Peckham, *et al.*, "64-tb/s (640× 107-gb/s) PDM-36QAM transmission over 320km using both pre-and post-transmission digital equalization," in *National Fiber Optic Engineers Conference*, p. PDPB9, Optical Society of America, 2010. DOI: https://doi.org/10.1364/NFOEC.2010.PDPB9.

[21] C. E. Shannon, "A mathematical theory of communication," *The Bell System Technical Journal*, vol. 27, no. 3, pp. 379–423, 1948. DOI: https://doi.org/10.1002/j.1538-7305.1948.tb01338.x.

[22] D. Menaka, S. Gauni, C. Manimegalai, and K. Kalimuthu, "Vision of IoUT: advances and future trends in optical wireless communication," *Journal of Optics*, pp. 1–14, 2021. DOI: https://doi.org/10.1007/s12596-021-00722-x.

[23] A. Chraplyvy, "The coming capacity crunch." [Plenary talk] presented at the *35th European Conference on Optical Communication*, Vienna, Austria, 2009. Available in: https://conference.vde.com/ecoc-2009/programs/documents/ecoc_final_program_15.09.09_web.pdf. Visited on: 09/06/2021.

[24] A. Ellis, N. M. Suibhne, D. Saad, and D. Payne, "Communication networks beyond the capacity crunch," *Philosophical Transactions of the Royal Society A*, vol. 374, no. 2062, p. 20150191, 2016. DOI: https://doi.org/10.1098/rsta.2015.0191.

[25] "Cisco annual internet report (2018–2023) white paper." Available in https://www.cisco.com/c/en/us/solutions/collateral/executive-perspectives/annual-internet-report/white-paper-c11-741490.html. Visited on 08/31/2020.

[26] D. Richardson, J. Fini, and L. E. Nelson, "Space-division multiplexing in optical fibres," *Nature Photonics*, vol. 7, no. 5, pp. 354–362, 2013. DOI: https://doi.org/10.1038/nphoton.2013.94.

[27] G. Li, N. Bai, N. Zhao, and C. Xia, "Space-division multiplexing: the next frontier in optical communication," *Advances in Optics and Photonics*, vol. 6, no. 4, pp. 413–487, 2014. DOI: https://doi.org/10.1364/AOP.6.000413.

[28] S. Inao, T. Sato, S. Sentsui, T. Kuroha, and Y. Nishimura, "Multicore optical fiber," in *Optical Fiber Communication Conference*, p. WB1, Optical Society of America, 1979. DOI: https://doi.org/10.1364/OFC.1979.WB1.

[29] S. Berdagué and P. Facq, "Mode division multiplexing in optical fibers," *Applied optics*, vol. 21, no. 11, pp. 1950–1955, 1982. DOI: https://doi.org/10.1364/AO.21.001950.

[30] T. Mizuno, H. Takara, A. Sano, and Y. Miyamoto, "Dense space division multiplexed transmission over multi-core and multi-mode fiber," in *2015 Optical Fiber Communications Conference and Exhibition (OFC)*, pp. 1–3, IEEE, 2015. DOI: https://doi.org/10.1364/OFC.2015.TH1D.2.

[31] L. Zhu, A. Wang, S. Chen, J. Liu, and J. Wang, "Orbital angular momentum mode multiplexed transmission in heterogeneous few-mode and multi-mode fiber network," *Optics letters*, vol. 43, no. 8, pp. 1894–1897, 2018. DOI: https://doi.org/10.1364/OL.43.001894.

[32] P. Sillard, M. Bigot-Astruc, D. Boivin, H. Maerten, and L. Provost, "Few-mode fiber for uncoupled mode-division multiplexing transmissions," in *2011 37th European Conference and Exhibition on Optical Communication*, pp. 1–3, IEEE, 2011. DOI: https://doi.org/10.1364/ECOC.2011.Tu.5.LeCervin.7.

[33] D. Gloge, "Weakly guiding fibers," *Applied Optics*, vol. 10, no. 10, pp. 2252–2258, 1971. DOI: https://doi.org/10.1364/ao.10.002252.

[34] G. B. Xavier and G. Lima, "Quantum information processing with space-division multiplexing optical fibres," *Communications Physics*, vol. 3, no. 1, pp. 1–11, 2020. DOI: https://doi.org/10.1038/s42005-019-0269-7.

[35] R. Ryf, S. Randel, A. H. Gnauck, C. Bolle, A. Sierra, S. Mumtaz, M. Esmaeelpour, E. C. Burrows, R.-J. Essiambre, P. J. Winzer, *et al.*, "Mode-division multiplexing over 96 km of few-mode fiber using coherent 6 × 6 MIMO processing," *Journal of Lightwave Technology*, vol. 30, no. 4, pp. 521–531, 2011. DOI: https://doi.org/10.1109/JLT.2011.2174336.

[36] J. van Weerdenburg, R. Ryf, J. C. Alvarado-Zacarias, R. A. Alvarez-Aguirre, N. K. Fontaine, H. Chen, R. Amezcua-Correa, T. Koonen, and C. Okonkwo, "138 tbit/s transmission over 650 km graded-index 6-mode fiber," in *2017 European Conference on Optical Communication (ECOC)*, pp. 1–3, IEEE, 2017. DOI: https://doi.org/10.1109/ECOC.2017.8346085.

[37] D. Soma, S. Beppu, Y. Wakayama, K. Igarashi, T. Tsuritani, I. Morita, and M. Suzuki, "257-Tbit/s weakly coupled 10-mode C + L-Band WDM transmission," *Journal of Lightwave Technology*, vol. 36, no. 6, pp. 1375–1381, 2018. DOI: https://doi.org/10.1109/JLT.2018.2792484.

[38] G. Rademacher, R. S. Luís, B. J. Puttnam, R. Ryf, H. Furukawa, R. Maruyama, K. Aikawa, A. Maruta, Y. Awaji, and N. Wada, "93.34 Tbit/s/mode (280 Tbit/s) transmission in a 3-mode graded-index few-mode fiber," in *Optical Fiber Communication Conference*, pp. W4C–3, Optical Society of America, 2018. DOI: https://doi.org/10.1364/OFC.2018.W4C.3.

[39] D. Soma, S. Beppu, S. Sumita, Y. Wakayama, T. Tsuritani, I. Morita, and M. Suzuki, "402.7-tb/s weakly-coupled 10-mode-multiplexed transmission using rate-adaptive PS PDM-16QAM WDM signals," in *45th European Conference on Optical Communication (ECOC 2019)*, pp. 1–4, IET, 2019. DOI: https://doi.org/10.1049/cp.2019.0909.

[40] S. Beppu, K. Igarashi, M. Kikuta, D. Soma, T. Nagai, Y. Saito, H. Takahashi, T. Tsuritani, I. Morita, and M. Suzuki, "Weakly coupled 10-mode-division multiplexed transmission over 48-km few-mode fibers with real-time coherent MIMO receivers," *Optics Express*, vol. 28, no. 13, pp. 19655–19668, 2020. DOI: https://doi.org/10.1364/OE.395415.

[41] R. Soref and J. Lorenzo, "Single-crystal silicon: a new material for 1.3 and 1.6 μm integrated-optical components," *Electronics Letters*, vol. 21, no. 21, pp. 953–954, 1985. DOI: https://doi.org/10.1049/el:19850673.

[42] E. Cortesi, F. Namavar, and R. Soref, "Novel silicon-on-insulator structures for silicon waveguides," in *IEEE SOS/SOI Technology Conference*, p. 109, IEEE, 1989. DOI: https://doi.org/10.1109/SOI.1989.69790.

[43] F. Namavar, E. Cortesi, R. Soref, and P. Sioshansi, "On the formation of thick and multiple layer simox structures and their applications," *MRS Online Proceedings Library*, vol. 147, no. 1, pp. 241–246, 1989. DOI: https://doi.org/10.1557/PROC-147-241.

[44] D. Thomson, A. Zilkie, J. E. Bowers, T. Komljenovic, G. T. Reed, L. Vivien, D. Marris-Morini, E. Cassan, L. Virot, J.-M. Fédéli, *et al.*, "Roadmap on silicon photonics," *Journal of Optics*, vol. 18, no. 7, p. 073003, 2016. DOI: https://doi.org/10.1088/2040-8978/18/7/073003.

[45] N. Margalit, C. Xiang, S. M. Bowers, A. Bjorlin, R. Blum, and J. E. Bowers, "Perspective on the future of silicon photonics and electronics," *Applied Physics Letters*, vol. 118, no. 22, p. 220501, 2021. DOI: https://doi.org/10.1063/5.0050117.

[46] L. H. Gabrielli, D. Liu, S. G. Johnson, and M. Lipson, "On-chip transformation optics for multimode waveguide bends," *Nature communications*, vol. 3, no. 1, pp. 1–6, 2012. DOI: https://doi.org/10.1038/ncomms2232.

[47] L. Gabrielli, D. Liu, S. Johnson, and M. Lipson, "On-chip multimode photonics," in *2012 Conference on Lasers and Electro-Optics (CLEO)*, pp. 1–2, IEEE, 2012. DOI: https://doi.org/10.1364/QELS.2012.QTh5B.4.

[48] J. B. Driscoll, R. R. Grote, B. Souhan, J. I. Dadap, M. Lu, and R. M. Osgood, "Asymmetric Y junctions in silicon waveguides for on-chip mode-division multiplexing," *Optics letters*, vol. 38, no. 11, pp. 1854–1856, 2013. DOI: https://doi.org/10.1364/OL.38.001854.

[49] Y.-D. Yang, Y. Li, Y.-Z. Huang, and A. W. Poon, "Silicon nitride three-mode division multiplexing and wavelength-division multiplexing using asymmetrical directional couplers and microring resonators," *Optics express*, vol. 22, no. 18, pp. 22172–22183, 2014. DOI: https://doi.org/10.1364/OE.22.022172.

[50] M. Zhang, H. Liu, B. Wang, G. Li, and L. Zhang, "Efficient grating couplers for space division multiplexing applications," *IEEE Journal of Selected Topics in Quantum Electronics*, vol. 24, no. 6, pp. 1–5, 2018. DOI: https://doi.org/10.1109/JSTQE.2018.2829659.

[51] D. Garcia-Rodriguez, J. L. Corral, A. Griol, and R. Llorente, "Bimodal grating coupler design on SOI technology for mode division multiplexing at 1550 nm," *Optics Express*, vol. 26, no. 15, pp. 19445–19455, 2018. DOI: https://doi.org/10.1364/OE.26.019445.

[52] L.-W. Luo, L. H. Gabrielli, and M. Lipson, "On-chip mode-division multiplexer," in *CLEO: 2013*, p. CTh1C.6, Optical Society of America, 2013. DOI: https://doi.org/10.1364/CLEO_SI.2013.CTh1C.6.

[53] L.-W. Luo, N. Ophir, C. P. Chen, L. H. Gabrielli, C. B. Poitras, K. Bergmen, and M. Lipson, "WDM-compatible mode-division multiplexing on a silicon chip," *Nature Communications*, vol. 5, no. 1, pp. 1–7, 2014. DOI: https://doi.org/10.1038/ncomms4069.

[54] D. Dai, C. Li, S. Wang, H. Wu, Y. Shi, Z. Wu, S. Gao, T. Dai, H. Yu, and H.-K. Tsang, "10-channel mode (de) multiplexer with dual polarizations," *Laser & Photonics Reviews*, vol. 12, no. 1, p. 1700109, 2018. DOI: https://doi.org/10.1002/lpor.201700109.

[55] P.-C. Kuo, Y. Tong, C.-W. Chow, J.-F. Tsai, Y. Liu, Y.-C. Chang, C.-H. Yeh, and H. K. Tsang, "4.36 Tbit/s silicon chip-to-chip transmission via few-mode fiber (FMF) using 2D sub-wavelength grating couplers," in *Optical Fiber Communication Conference*, pp. M3D–6, Optical Society of America, 2021. URL: http://www.osapublishing.org/abstract.cfm?URI=OFC-2021-M3D.6.

[56] A. E. Siegman, "Defining, measuring, and optimizing laser beam quality," in *Laser Resonators and Coherent Optics: Modeling, Technology, and Applications*, vol. 1868, pp. 2–12, International Society for Optics and Photonics, 1993. DOI: https://doi.org/10.1117/12.150601.

[57] J. Nilsson, J. K. Sahu, Y. Jeong, W. A. Clarkson, R. Selvas, A. B. Grudinin, and S. Alam, "High-power fiber lasers: new developments," in *Advances in Fiber Lasers*, vol. 4974, pp. 50–59, International Society for Optics and Photonics, 2003. DOI: https://doi.org/10.1117/12.478310.

[58] J. Limpert, A. Liem, H. Zellmer, , and A. Tunnermann, "500 w continuous-wave fibre laser with excellent beam quality," *Electronics Letters*, vol. 39, no. 8, pp. 645–647, 2003. DOI: https://doi.org/10.1049/el:20030447.

[59] H. Yoda, P. Polynkin, and M. Mansuripur, "Beam quality factor of higher order modes in a step-index fiber," *Journal of lightwave technology*, vol. 24, no. 3, p. 1350, 2006. DOI: https://doi.org/10.1109/JLT.2005.863337.

[60] S. Wielandy, "Implications of higher-order mode content in large mode area fibers with good beam quality," *Optics Express*, vol. 15, no. 23, pp. 15402–15409, 2007. DOI: https://doi.org/10.1364/OE.15.015402.

[61] O. Shapira, A. F. Abouraddy, J. D. Joannopoulos, and Y. Fink, "Complete modal decomposition for optical waveguides," *Physical review letters*, vol. 94, no. 14, p. 143902, 2005. DOI: https://doi.org/10.1103/PhysRevLett.94.143902.

[62] T. Kaiser, B. Lüdge, S. Schröter, D. Kauffmann, and M. Duparré, "Detection of mode conversion effects in passive LMA fibers by means of optical correlation analysis," in *Solid State Lasers and Amplifiers III*, vol. 6998, p. 69980J, International Society for Optics and Photonics, 2008. DOI: https://doi.org/10.1117/12.783100.

[63] T. Kaiser, D. Flamm, S. Schröter, and M. Duparré, "Complete modal decomposition for optical fibers using CGH-based correlation filters," *Optics Express*, vol. 17, no. 11, pp. 9347–9356, 2009. DOI: https://doi.org/10.1364/OE.17.009347.

[64] T.-J. Ahn and D. Kim, "High-resolution differential mode delay measurement for a multimode optical fiber using a modified optical frequency domain reflectometer," *Optics Express*, vol. 13, no. 20, pp. 8256–8262, 2005. DOI: https://doi.org/10.1364/OPEX.13.008256.

[65] S. Ring, D. Menashe, U. Levy, S. Steinblatt, Y. Danziger, and M. Tur, "Characterization of mode coupling in few-mode fibers using optical low-coherence reflectometry," in *Optical Fiber Communication Conference*, p. OWO5, Optical Society of America, 2008. DOI: https://doi.org/10.1109/OFC.2008.4528751.

[66] D. Schimpf, R. Barankov, and S. Ramachandran, "Cross-correlated (c 2) imaging of fiber and waveguide modes," *Optics Express*, vol. 19, no. 14, pp. 13008–13019, 2011. DOI: https://doi.org/10.1364/OE.19.013008.

[67] S. Ramachandran, J. Nicholson, S. Ghalmi, and M. Yan, "Measurement of multipath interference in the coherent crosstalk regime," *IEEE Photonics Technology Letters*, vol. 15, no. 8, pp. 1171–1173, 2003. DOI: https://doi.org/10.1109/LPT.2003.814880.

[68] J. Nicholson, A. D. Yablon, S. Ramachandran, and S. Ghalmi, "Spatially and spectrally resolved imaging of modal content in large-mode-area fibers," *Optics Express*, vol. 16, no. 10, pp. 7233–7243, 2008. DOI: https://doi.org/10.1364/OE.16.007233.

[69] J. Nicholson, L. Meng, J. Fini, R. Windeler, A. DeSantolo, E. Monberg, F. DiMarcello, Y. Dulashko, M. Hassan, and R. Ortiz, "Measuring higher-order modes in a low-loss, hollow-core, photonic-bandgap fiber," *Optics Express*, vol. 20, no. 18, pp. 20494–20505, 2012. DOI: https://doi.org/10.1364/OE.20.020494.

[70] D. M. Nguyen, S. Blin, T. N. Nguyen, S. D. Le, L. Provino, M. Thual, and T. Chartier, "Modal decomposition technique for multimode fibers," *Applied Optics*, vol. 51, no. 4, pp. 450–456, 2012. DOI: https://doi.org/10.1364/AO.51.000450.

[71] E. A. Lamilla Rubio, *Characterization and manipulation of optical modes in photonic crystal fibers*. PhD thesis, Universidade Estadual de Campinas, Instituto de Física Gleb Wataghin, Campinas, SP, 2019.

[72] E. Lamilla, M. S. Faria, I. Aldaya, P. F. Jarschel, J. L. Pita, and P. Dainese, "Characterization of surface-states in a hollow core photonic crystal fiber," *Optics Express*, vol. 26, no. 25, pp. 32554–32564, 2018. DOI: https://doi.org/10.1364/OE.26.032554.

[73] K. Okamoto, *Fundamentals of Optical Waveguides*. Elsevier, second ed., 2006.

[74] H. R. Sunak and S. P. Bastien, "Refractive index and material dispersion interpolation of doped silica in the 0.6–1.8 μm wavelength region," *IEEE Photonics Technology Letters*, vol. 1, no. 6, pp. 142–145, 1989. DOI: https://doi.org/10.1109/68.36016.

[75] H. Wehr and D. Wiechert, "Refractive index and density of fluorine doped silica prepared by the pcvd process," *Materials research bulletin*, vol. 21, no. 5, pp. 559–566, 1986. DOI: https://doi.org/10.1016/0025-5408(86)90110-8.

[76] J. L. P. Ruiz, L. G. Rocha, J. Yang, Ş. E. Kocabaş, M.-J. Li, I. Aldaya, P. Dainese, and L. H. Gabrielli, "Efficient integrated tri-modal coupler for few-mode fibers," *Optics*

Express, vol. 30, no. 2, pp. 2539–2546, 2022. DOI: https://doi.org/10.1364/OE.446097.

[77] L. Chrostowski and M. Hochberg, *Silicon Photonics Design*. Cambridge University Press, 2015.

[78] T. Watanabe, Y. Fedoryshyn, and J. Leuthold, "2-d grating couplers for vertical fiber coupling in two polarizations," *IEEE Photonics Journal*, vol. 11, no. 4, pp. 1–9, 2019. DOI: https://doi.org/10.1109/JPHOT.2019.2926823.

Appendix A

Numerical differentiation at three points

A.1 Calculation of the first derivative

The function $\beta(\omega)$ is not known, but the values of this function at specific points are in a such way that $\beta(\omega_1) = \beta_1$, $\beta(\omega_2) = \beta_2$ and $\beta(\omega_3) = \beta_3$. Applying Taylor series, it follows that:

$$\beta_1 = \beta_2 - \beta'(\omega_2)\Delta\omega_{21} + \beta''(\omega_2)\frac{\Delta\omega_{21}^2}{2} + O(\Delta\omega^3) \tag{A.1}$$

$$\beta_3 = \beta_2 + \beta'(\omega_2)\Delta\omega_{32} + \beta''(\omega_2)\frac{\Delta\omega_{32}^2}{2} + O(\Delta\omega^3) \tag{A.2}$$

$$\Delta\omega_{21} = \omega_2 - \omega_1,\ \Delta\omega_{32} = \omega_3 - \omega_2$$

Where $\beta' = d\beta/d\omega$ is the first derivative of β with respect to ω, and $\beta'' = d^2\beta/d\omega^2$ is the second derivative of β with respect to ω. Eliminating terms with $\beta''(\omega_2)$ and isolating $\beta'(\omega_2)$, it follows that:

$$\beta'(\omega_2) = \beta_2' = \frac{[\Delta\omega_{21}^2(\beta_3 - \beta_2) + \Delta\omega_{32}^2(\beta_2 - \beta_1)]}{[\Delta\omega_{32}\Delta\omega_{21}(\omega_3 - \omega_1)]} + O(\Delta\omega^2) \tag{A.3}$$

The term $O(\Delta\omega^2)$ is the truncation error.

A.2 Calculation of the second derivative

Doing the same initials considerations and using the expanded Taylor series eq. (A.1) and eq. (A.2). Now, eliminate terms with $\beta'(\omega_2)$ and isolate $\beta''(\omega_2)$, such that:

$$\beta''(\omega_2) = \beta_2'' = \frac{2\,[\beta_1\Delta\omega_{32} - \beta_2(\Delta\omega_{21} + \Delta\omega_{32}) + \beta_3\Delta\omega_{21}]}{[\Delta\omega_{21}\Delta\omega_{32}(\Delta\omega_{21} + \Delta\omega_{32})]} + O(\Delta\omega^2) \tag{A.4}$$